Numerical Block-Based Simulation of Rocking Structures Using a Novel Universal Viscous Damping Model

Georgios Vlachakis[1]; Anastasios I. Giouvanidis[2]; Anjali Mehrotra[3]; and Paulo B. Lourenço[4]

Abstract: Unreinforced masonry structures, particularly façade walls, are seismically vulnerable due to their weak connections with adjacent walls, floors, and/or roofs. During an earthquake, such walls formulate local mechanisms prone to out-of-plane collapse. This behavior has been largely investigated using classical rocking theory, which assumes the structure responds as a rigid body undergoing rocking motion, with energy dissipation at impact. Due to the complexity of the problem, however, e.g., number of degrees of freedom or boundary conditions, numerical block-based modeling is gaining momentum. However, numerical models lack a consistent and reliable treatment of the energy loss at impact. This paper bridges the gap between the well-established energy loss of classical rocking theory and the treatment of damping in numerical modeling. Specifically, it proposes an equivalent viscous damping model through novel ready-to-use predictive equations that capture the dissipative phenomena during both one-sided and two-sided planar rocking motion. The results reveal a satisfactory performance of the proposed model through comparisons with experimental results from literature and highlight its universality and robustness through applications of the model in fundamentally different block-based numerical modeling software. **DOI: 10.1061/(ASCE)EM.1943-7889.0001985.**

Author keywords: Rocking; Coefficient of restitution; Viscous damping; Numerical modeling; Out-of-plane collapse.

Introduction

Masonry structures display high vulnerability to seismic action—threatening human lives, built assets, and a major part of our cultural heritage (Bruneau 1994; Penna et al. 2014). Among the observed types of failure, out-of-plane (OOP) collapse is the most frequent—particularly in the case of façade walls with poor connections to transversal elements or diaphragms (Ingham and Griffith 2011; Vlachakis et al. 2020, among others). Analysis of these OOP collapse mechanisms is typically conducted using simplified limit analysis procedures (D'Ayala and Speranza 2003; Vaculik et al. 2014), whereby the capacity of the mechanisms is evaluated through calculation of an equivalent static lateral force required to trigger each mechanism and eventually cause collapse of the structure. However, forced-based approaches can be overconservative because they tend to neglect the dynamic reserve of stability, particularly in the case of large-scale structures, which undergo significant displacements before overturning (Godio and Beyer 2019; Sorrentino et al. 2017).

To that end, the employment of theoretical rocking dynamics has been proposed to evaluate the OOP dynamic stability of masonry walls (e.g., Casapulla et al. 2017 and references therein). Following Housner's (1963) seminal work on the single rigid rocking block, the equations that describe the motion of masonry walls (simulated as rigid blocks) have been developed using rocking (Lagrangian) dynamics. Furthermore, the influence on the response of both seismological parameters (Giouvanidis and Dimitrakopoulos 2018) and certain structural characteristics, such as the presence of additional loads due to, e.g., masses from floor and/or roof elements, or thrust from vaults (Giresini et al. 2015; Mauro et al. 2015), tie bars (AlShawa et al. 2019; Mauro et al. 2015), and transverse walls (Giresini and Sassu 2017; Al Shawa et al. 2012; Sorrentino et al. 2011), as well as the formulation of a two-block mechanism, which occurs in the case of walls restrained by floors or a roof (Mauro et al. 2015; Sorrentino et al. 2011) has been extensively investigated.

In such a methodological framework, energy dissipation is assumed to occur entirely at impact, and is accounted for by the coefficient of restitution (COR) which correlates the angular velocity of the structure before and after impact. The COR may be determined analytically through the assumption of conservation of angular momentum, after specifying the geometry of the block and the points of impact (Hogan 1992; Housner 1963). Experimental investigations have evaluated the accuracy of the COR calculated using the classical rocking theory, and despite some discrepancies observed, it appears that the overall energy loss of rocking blocks can be adequately captured (Bachmann et al. 2018; Cappelli et al. 2020; Chatzis et al. 2017; Costa et al. 2013; Kalliontzis and Sritharan 2018; Lipscombe and Pellegrino 1993). However, as the complexity of the structure increases, e.g., more degrees of freedom, different boundary conditions, or introduction of flexible interfaces, among others, the classical rocking theory becomes complicated. Thus, alternative analytical and numerical models

[1]Ph.D. Candidate, Institute for Sustainability and Innovation in Structural Engineering, Dept. of Civil Engineering, Univ. of Minho, Guimarães 4800-058, Portugal. Email: giorgovlachaki@gmail.com

[2]Postdoctoral Fellow, Institute for Sustainability and Innovation in Structural Engineering, Dept. of Civil Engineering, Univ. of Minho, Guimarães 4800-058, Portugal (corresponding author). ORCID: https://orcid.org/0000-0002-5850-3095. Email: agiouvanidis@civil.uminho.pt

[3]Postdoctoral Fellow, Institute for Sustainability and Innovation in Structural Engineering, Dept. of Civil Engineering, Univ. of Minho, Guimarães 4800-058, Portugal. ORCID: https://orcid.org/0000-0002-3453-2879. Email: amehrotra@civil.uminho.pt

[4]Professor, Institute for Sustainability and Innovation in Structural Engineering, Dept. of Civil Engineering, Univ. of Minho, Guimarães 4800-058, Portugal. Email: pbl@civil.uminho.pt

Note. This manuscript was submitted on January 11, 2021; approved on May 11, 2021; published online on August 24, 2021. Discussion period open until January 24, 2022; separate discussions must be submitted for individual papers. This paper is part of the ***Journal of Engineering Mechanics***, © ASCE, ISSN 0733-9399.

have been proposed to capture the transient nonlinear dynamic response of various rocking configurations (Giouvanidis and Dimitrakopoulos 2017a; Mehrotra and Dejong 2020; Spanos et al. 2001).

At the same time, recent developments in computational approaches used for modeling masonry structures are gaining momentum, particularly block-based models, which have been found capable of reproducing the dynamic response of masonry walls while also being able to model masonry texture and interaction with surrounding structural elements. These include the finite-element (FE) method (D'Altri et al. 2019), the discrete-element (DE) method (Lemos 2019), and multibody dynamics (Portioli and Cascini 2018). However, despite their widespread use, applications of these models usually lack a reliable treatment of the energy loss due to the nonsmooth behavior of impacts during rocking motion (de Felice et al. 2017; Sarhosis et al. 2019; Vassiliou et al. 2021). Thus, viscous damping models are usually adopted. Viscous models are mathematical artifices with a continuous nature, seemingly in complete contrast with the impulsive energy loss suggested by the classical rocking theory. This characteristic appears to be a source of uncertainty in numerical simulations of rocking bodies (AlShawa et al. 2017; Lemos and Campos Costa 2017; Malomo et al. 2021), making damping one of the main parameters that needs to be adjusted to obtain a better fit to a reference response rather than a quite consistent method, such as the classical rocking theory (Housner 1963).

The main objective of the present study is to bridge the gap between the well-established energy loss of the classical rocking theory (Housner 1963) and the treatment of damping of block-based numerical models. This is conducted following a phenomenological calibration of a viscous damping model to mimic the classical rocking (COR) theory, and pertinent ready-to-use expressions are proposed. More specifically, two of the most common problems evident in masonry structures are investigated: two-sided and one-side rocking (Fig. 1).

Two-sided rocking behavior represents the motion of a parapet, gable or boundary wall rocking over their foundation when subjected to ground excitation, whereas one-sided rocking behavior describes the motion of masonry façades with insufficient connections to transversal walls. Through a series of over a thousand numerical simulations, this work proposes ready-to-use expressions that agree with the well-established classical rocking theory and efficiently capture the energy loss during rocking motion of any numerical block-based structure. Importantly, the results of this study serve as the basis for a more rational and holistic approach to model (1) multi-degree-of-freedom rocking structures, (2) the interaction of complex geometries and boundary conditions with the rocking response, and (3) the inclusion of material nonlinearities.

To this end, the main dynamic characteristics of both approaches, i.e., classical rocking theory and the numerical block-based modeling, are firstly outlined, paving the way for an appropriate selection of the viscous damping model. During the calibration process of the proposed viscous damping model, special attention is given to its universality via its application in fundamentally different numerical modeling software, as well as its capability of including modifications of the classical rocking theory suggested by previous experimental and theoretical studies (e.g., Kalliontzis et al. 2016; Sorrentino et al. 2011; Ther and Kollar 2017, among others). Finally, the performance of the proposed numerical viscous damping model is evaluated against experimental campaigns available in literature, highlighting both its merits and shortcomings.

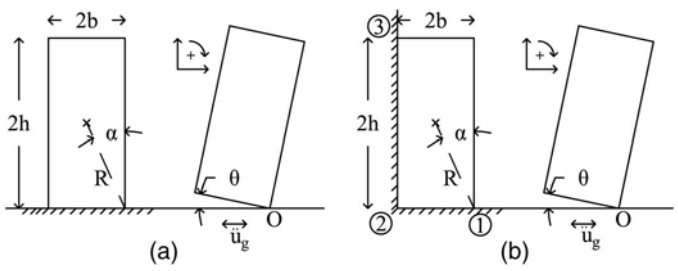

Fig. 1. Archetypal rocking block exhibiting (a) two-sided rocking motion; and (b) one-sided rocking motion when subjected to horizontal ground excitation.

Analytical Modeling of Rocking Structures

In principle, during a strong ground motion, rocking action activates the structure's rotational inertia and offers a favorable seismic isolation effect, which relieves the structure from deformation and ultimately damage. Rocking becomes evident in a variety of structural configurations, e.g., from bridges (Giouvanidis and Dimitrakopoulos 2017b; Giouvanidis and Dong 2020; Routledge et al. 2020) and buildings (Bachmann et al. 2017) to cultural heritage structures (Mehrotra and DeJong 2018) and classical monuments (Di Egidio and Contento 2009; Psycharis et al. 2013). However, the main concern in rocking dynamics is the existence of large displacements (or equivalently rotations) during rocking motion, which might cause instability and eventually overturning of the structure. Therefore, the associated challenges behind this peculiar seismic behavior should be properly addressed with advanced analytical and numerical simulations that can capture with high fidelity the transient nonlinear dynamic behavior of rocking structures.

Consider the rocking block of Fig. 1 standing free on a rigid ground. During an earthquake, rocking commences when the seismic demand due to the horizontal ground excitation becomes equal to the seismic resistance due to the gravitational and inertial forces acting on the body. This condition yields the minimum ground acceleration necessary for rocking to initiate $\ddot{u}_{g,\min} = g \cdot \tan(\alpha)$ (Housner 1963), where g is the acceleration of gravity and α is the slenderness of the block $\alpha = \arctan(b/h)$ (Fig. 1).

After rocking initiates, the equation that describes the motion of the rocking block of Fig. 1 can be expressed as follows (Housner 1963):

$$\ddot{\theta} = -p^2\left[\sin(\pm\alpha - \theta) + \frac{\ddot{u}_g}{g}\cos(\pm\alpha - \theta)\right] \tag{1}$$

where $\ddot{u}_g$ = (horizontal) ground acceleration; positive and negative signs = clockwise and counterclockwise rotation θ, respectively; and p = frequency parameter of the block, defined as $p = \sqrt{mgR/I_0}$ with m representing the mass of the block, and I_0 representing the rotational moment of inertia with respect to the pivot points. In the case of a rectangular block, p simplifies to $p = \sqrt{3g/4R}$, where R is the diagonal distance from the center of mass of the block to the pivot point (Fig. 1).

The importance of the parameter p, being inversely proportional to the square root of the size R, has been studied in the past (e.g., Makris 2014, among others). From a physical perspective, the frequency parameter p refers to the pendulum frequency of the block as if it is hanging from its pivot point (DeJong and Dimitrakopoulos 2014), and not the classical natural frequency, which usually measures cycles of vibration per second. This discrepancy stems from the fact that the natural frequency and period

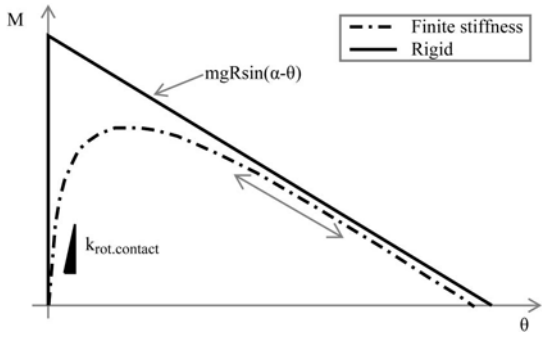

Fig. 2. Moment-rotation relationship of the rocking block of Fig. 1 based on the classical rocking theory and more realistic nonlinear numerical modeling with finite stiffness. (Data from Housner 1963.)

of the rocking motion is amplitude dependent, and thus, unsuitable for characterizing a structure (Housner 1963)

$$T_{\text{rock}} = \frac{4}{p}\cosh^{-1}\left(\frac{1}{1-\frac{\theta_0}{\alpha}}\right) \tag{2}$$

During rocking, the smooth motion of the block is interrupted by nonsmooth impacts at its contact/pivot points. The classical rocking theory (Housner 1963) considers impact as an instantaneous event, where the system is characterized by infinite stiffness (Fig. 2). When impact occurs, energy is lost. Ignoring bouncing and assuming the block sustains pure rocking motion (i.e., no sliding at the contact interface), the energy loss at impact is captured by COR, e, acting as radiation damping. The COR connects the preimpact with the postimpact angular velocity $e = \dot{\theta}^{+}/\dot{\theta}^{-}$.

When the rectangular block of Fig. 1(a) undergoes two-sided rocking motion (denoted as 2s henceforth), conservation of angular momentum yields (Housner 1963)

$$e_{2s,an} = 1 - \frac{3}{2}\sin^2\alpha \tag{3}$$

From Eq. (3), COR depends entirely upon the geometry (i.e., slenderness) of the block. Thus, the material properties (e.g., mass or stiffness) are irrelevant to the damping phenomenon during impact.

However, there are cases where the block during its smooth rocking motion, apart from the impact with the ground, also comes into contact with an adjacent wall representing masonry façades inadequately connected with the transversal walls. In such cases, the block exhibits one-sided rocking motion (denoted as 1s henceforth) as shown in Fig. 1(b). Bao and Konstantinidis (2020) treated the impact with the adjacent sidewall as an additional event characterized by a separate/independent COR. Similarly, Sorrentino et al. (2011) assumed three consecutive impacts taking place in close but distinct time instants. Specifically, an impact at the base of the block [i.e., Point 2 in Fig. 1(b)], followed by an impact at the upper corner [i.e., Point 3 in Fig. 1(b)], and finally an additional impact at the base [i.e., Point 1 in Fig. 1(b)], resulting in a postimpact rocking rotation around the same pivot point as the preimpact rocking rotation but in the opposite direction (i.e., $\dot{\theta}^{+}/\dot{\theta}^{-} < 0$). Under these assumptions, COR, which captures the impact of the rectangular rocking block of Fig. 1(b) with the transverse wall utilizing conservation of angular momentum, becomes

$$e_{tr,an} = 1 - \frac{3}{2}\cos^2\alpha \tag{4}$$

Therefore the total energy loss when the block of Fig. 1(b) undergoes one-sided rocking motion can be expressed as a lumped COR considering all three impacts (Sorrentino et al. 2011)

$$e_{1s} = e_{2s}^2 \cdot e_{tr} \tag{5}$$

Numerical Modeling of Rocking Structures

From a numerical perspective, modeling the behavior of the rocking structure of Fig. 1 is challenging, mainly due to the presence of finite interface stiffness (as opposed to the theoretically infinite interface stiffness of the classical rocking theory) and the nonsmooth nature of impacts.

Interface Stiffness

When simulating the rocking response using numerical block-based models, normal and tangential stiffness (k_n and k_s) are introduced at the corresponding interfaces to capture the interaction of the contacting bodies. The introduction of the interface stiffness facilitates the modeling of additional macroscale characteristics of the rocking problem, such as rough-gap closure stiffness (Lourenço et al. 2005), material elasticity (Acikgoz and DeJong 2012; Avgenakis and Psycharis 2017; Vassiliou et al. 2014), foundation flexibility (Spanos et al. 2017), or even wall degradation (Griffith et al. 2004). Subsequently, the moment-rotation (or equivalently force-displacement) diagram has the form shown in Fig. 2 (Costa et al. 2013; Giordano et al. 2020; Godio and Beyer 2017; Mehrotra and Dejong 2020). More specifically, the nonlinear curve is characterized by an initial elastic part that corresponds to the full contact phase, a plateaulike part where rocking around a pivot point occurs, and a softening part that, due to the geometrically nonlinear nature of the problem, converges to the theoretically softening part of the rigid body.

Based on Fig. 2, the initial rotational contact stiffness ($k_{\text{rot·contact}}$) of the block can be expressed

$$k_{\text{rot.contact}} = \frac{1}{12}k_n(2b)^3(2l) \tag{6}$$

where $(2b)$ = block's width (Fig. 1); and $(2l)$ = block's depth in the general three-dimensional (3D) configuration. The normal stiffness k_n is distributed over the area of the interface and consequently has units of Newtons per cubic meter.

Recall that the dynamic rocking response of a numerical model with finite stiffness is slightly different from the classical rocking theory (Housner 1963), specifically with regard to the treatment of impact. In contrast with the assumptions of instantaneous duration of impact and infinite normal stiffness during full contact, the numerical model presents finite stiffness, and thus, impact occurs over finite displacement and time. Hence, the rotational contact/impact frequency can be approximated as follows:

$$f_{\text{rot.contact}} \simeq \frac{1}{2\pi}\sqrt{\frac{k_{\text{rot.contact}}}{I_{\text{rot·}}}} \tag{7}$$

where $I_{\text{rot·}}$ = rotational mass moment of inertia about the center of the interface section. For brevity, influence of potential overburden weight at the section (i.e., stress stiffening effect), block deformability, and geometrical nonlinearity are neglected. Evidently, the finite stiffness model experiences a huge stiffness increase during impact (i.e., when contact occurs), which lasts for the short time interval until the block changes pivot point and continues rocking

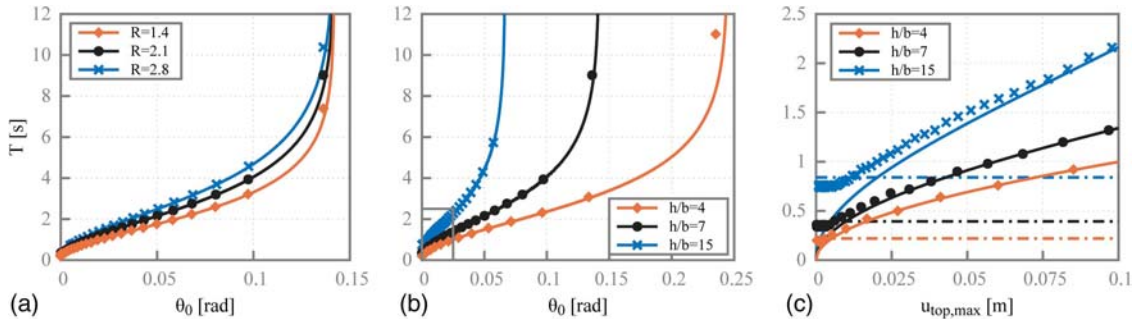

Fig. 3. Period of vibration with respect to the rocking amplitude for rocking blocks with different (a) scale R; (b) slenderness (or aspect ratio) h/b; and (c) period of vibration with respect to maximum top displacement for the area denoted in plot b.

$$f_{\text{rot.contact}} \gg \frac{1}{T_{\text{rock}}} \tag{8}$$

To illustrate the overall similarity between the analytical rigid model and the numerical finite stiffness model, Fig. 3 plots the nonlinear dependency of the rocking period described by Eq. (2) with solid lines, and a set of points marks the response of the numerical finite stiffness model for different values of the scale R and slenderness (i.e., aspect ratio) $h/b[= 1/\arctan(\alpha)]$. Overall, Fig. 3 shows good agreement between the rigid and finite stiffness model. The small difference observed at higher amplitudes stems from the small shrinkage of the negative stiffness part in the moment-rotation diagram (Fig. 2). This is an additional attribute introduced by the finite stiffness model, which arises by a slight inward shift of the pivot point at the base during rocking.

Fig. 3(c) plots the analytical expression of Eq. (2) with respect to the top displacement (instead of rotation) of the block. Specifically, Fig. 3(c) provides a closer look at the bottom-left corner of Fig. 3(b), illustrating the difference of the examined models during contact and the influence of the finite stiffness of the numerical model compared with the theoretically infinite stiffness of the analytical rigid model. The response of the finite stiffness model does not converge to the axis' origin, but stops on a finite period. Fig. 3(c) also plots the period of vibration ($T_{\text{rot·contact}} = 1/f_{\text{rot·contact}}$) of Eq. (7) (dashed horizontal lines). Importantly, Fig. 3(c) illustrates the very good estimation of the contact frequency that Eq. (7) provides despite the adopted simplifications. The limit frequency shown in Fig. 3(c), and analytically expressed through Eq. (7), is in agreement with a recent experimental campaign on the (two-sided) rocking behavior of masonry walls (Cappelli et al. 2020).

Energy Dissipation

Numerical models also treat energy dissipation in a different manner from the classical rocking theory (Housner 1963). Specifically, instead of the instantaneous event-based approach that the classical rocking theory assumes, energy loss is regarded as a continuous process throughout rocking motion, usually simulated via a viscous definition or a hysteretic constitutive relationship (Charney 2008). However, such damping models are not intended to describe the micromechanical nature of the phenomena taking place, but rather reproduce the overall dissipation in a phenomenological fashion. To this end, calibration methodologies are employed that tune the damping model to produce the desired response.

Viscous damping models are mathematical artifices employed to simulate sources of dissipation (such as damping radiation at impact) that are not modeled explicitly in their physical sense, yet are important enough at the structural system's level to not be ignored (Hall 2006). By definition, viscous models assume that the damping forces are proportional to the velocity of the structural system through the damping coefficient $\mathbf{C}$. This provides a mathematical convenience to simulate the energy dissipation because velocity is out of phase with displacement and acceleration. Different viscous damping models have been proposed, which mainly differ based on (1) the degrees of freedom (DOFs) of the velocity vector upon which $\mathbf{C}$ acts, (2) the way $\mathbf{C}$ behaves during time-history analyses, and (3) the exact value of $\mathbf{C}$.

Damping can be treated as a material characteristic assigned at each DOF of the structure, where the dissipation process is distributed along the structure. Alternatively, damping can also be treated as a dashpot assigned at specific DOFs and act locally on the relative velocity between two nodes. Considering the localized nature of the rocking problem, the dashpot definition appears to be a more viable solution. In addition, several viscous damping definitions have been proposed to describe the energy dissipation during the response-history of a structure. Fig. 4 illustrates the most widely used.

In particular, the constant damping coefficient (CDC) model retains the same value of $\mathbf{C}$ throughout the response history. This is equivalent to a mass-proportional Rayleigh damping definition, thus damping out low-frequency content. Another well-established model associates a constant damping ratio (CDR) with all frequencies. This definition allows an update of the stiffness matrix but not the damping ratio ξ during the response history, resulting in an equivalent dissipation of all the frequency content. Further, a stiffness-proportional damping ratio (SDR) allows the damping ratio ξ to follow the changes of the stiffness matrix during the response history. As a result, the high-frequency content of the

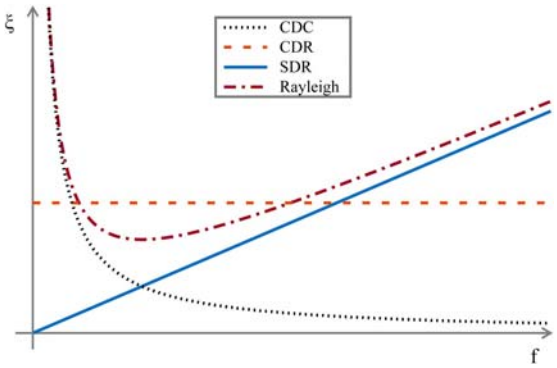

Fig. 4. Different viscous damping models with respect to the frequency content.

Table 1. Summary of available ξ-e relationships in literature applicable to the rocking problem

Reference	Relationship	Basic assumptions
Priestley et al. (1978)	$\xi = \frac{1}{n \cdot \pi} \ln\left\{ \frac{\theta_0}{\alpha} \left[1 - \sqrt{1 - e^{2n} \left[1 - \left(1 - \frac{\theta_0}{\alpha} \right)^2 \right]} \right]^{-1} \right\}$	Equivalence between COR theory and viscous decay of elastic oscillator
Makris and Konstantinidis (2003)	$\xi = -0.68 \cdot \ln(e)$	Simplified approximation of the Priestley et al. (1978) relationship
Giannini and Masiani (1990)	$\xi = \frac{2 \cdot (1 - e)}{\pi \cdot (1 + e)}$	Equivalence between COR theory and viscous energy loss of unilateral dashpot
Anagnostopoulos (2004)	$\xi = -\frac{\ln(e)}{\sqrt{\pi^2 + (\ln(e))^2}}$	Equivalence between COR theory and viscous energy loss of unilateral dashpot
Imanishi et al. (2012)	$\xi = -\frac{\ln(e)}{\sqrt{4 \cdot \pi^2 + (\ln(e))^2}}$	Equivalence between COR theory and viscous energy loss of unilateral dashpot
Cheng (2007)	$\xi = \frac{(1 - e^2)}{\pi \cdot (1 - \Delta/b)}$	Equivalence between COR theory and viscous energy loss
DeJong (2009)	$\xi = \frac{b}{2 \cdot h}; \xi = \frac{b}{R}; \xi = 100\%$	Alternative proposals for spring dashpots at corners of discrete model
Tomassetti et al. (2019)	$\xi = -0.218 \cdot a_1 - 0.195 \cdot \ln(e)$	Equivalence between COR theory and a SDOF analytical formulation with viscous energy loss

Note: n = number of impacts; Δ/b = amplitude of motion; SDOF = single degree of freedom; and a_1 = alternative definition of system's stiffness based on a trilinear force-displacement relationship.

response is highly dissipated. Finally, a combination of both mass and stiffness proportional models acting at the same time, known as Rayleigh damping, damps out both the low and high range of the frequency content (Fig. 4).

During rocking, when impact occurs, a huge increase in the frequency content takes place [Eq. (7)] for a very short, yet finite, time and displacement. Therefore, the SDR definition presents a convenient approach to model the damping of rocking structures. Physically speaking, if the SDR definition is used together with a dashpot model, unilateral behavior of the dashpot is achieved, i.e., energy is dissipated only when the dashpot is in contact.

In addition, a proper treatment of impact requires a proper definition of the value of $\mathbf{C}$ (or equally, the value of ξ). Particularly for the rocking problem, a relationship between the coefficient of restitution e and damping ratio ξ is critical to ensure energy equivalence between the classical rocking theory (Housner 1963) and the numerical viscous damping model. Table 1 provides a summary of the ξ–e relationships available in literature applicable to the rocking problem accompanied by their basic assumptions. More specifically, Priestley et al. (1978) first examined the energy loss equivalence of the classical impulsive dynamics theory and the viscous decay of an elastic oscillator. Later, Makris and Konstantinidis (2003) simplified the ξ–e expression of Priestley et al. (1978), assuming damping independent of the rocking amplitude. Anagnostopoulos (2004) studied the energy equivalence between the COR and a spring-dashpot viscous model based on the two colliding masses scheme, and Giannini and Masiani (1990) and Imanishi et al. (2012) proposed equivalent formulations. DeJong (2009) simulated the rocking block with corner spring-dashpots adopting a SDR damping formulation to critically damp either the axial frequency, the corner frequency, or the rotational frequency. Recently, Tomassetti et al. (2019) followed a calibration process of a single degree of freedom (SDOF) analytical formulation of rocking structures adopting different formulations of viscous models (i.e., CDC, CDR, and SDR), and the influences on the response of additional parameters, such as the interface stiffness, rocking amplitude, and aspect ratio, were also investigated.

Importantly, the aforementioned proposals are based either on simplified SDOF analytical schemes (Anagnostopoulos 2004; Giannini and Masiani 1990; Imanishi et al. 2012; Priestley et al. 1978; Tomassetti et al. 2019) or their equivalence with the COR has been omitted (DeJong 2009). In fact, a meticulous investigation on the energy loss equivalence between the viscous damping model used in block-based numerical simulations and the classical rocking (COR) theory is still lacking from the literature, despite the widespread use of numerical models in the last decades.

Adopted Viscous Damping Model

The main objective of the present work is to adopt a viscous damping model that is able to reproduce with high fidelity the impulsive dynamics' energy loss characteristics and subsequently ensure dynamic equivalence between the classical rocking theory (Housner 1963) and the numerical viscous damping model in a universal manner, i.e., applicable to different rocking structures of different materials simulated in different finite-element/discrete-element software. Recall that a unilateral dashpot definition provides the most convenient basis to meet this goal. This section provides a closer look at the performance of the adopted viscous damping model through a series of free-rocking simulations of the structure shown in Fig. 1 undergoing both two-sided and one-sided rocking motion.

The analytical model adopted herein is based on the classical rocking theory (Housner 1963). Specifically, an event-based approach is adopted, according to which the motion of the rocking block of Fig. 1 can be decomposed into a smooth motion interrupted by nonsmooth contact events (i.e., impacts). The smooth rocking motion of the block is obtained through the solution of the differential equation of Eq. (1) using mathematical programming in MATLAB version 2017a (MathWorks 1992). Whenever impact occurs, the integration stops and the coefficient of restitution [Eq. (3) for the two-sided rocking case or Eq. (5) for the one-sided rocking case] is applied to determine the new initial conditions for the next iteration.

The same problem is also formulated in a finite element environment, i.e., ABAQUS CAE version 2019 (Simulia 2012), a widely used FEM software well-suited for block-based simulations that include contact phenomena. A schematic representation of the

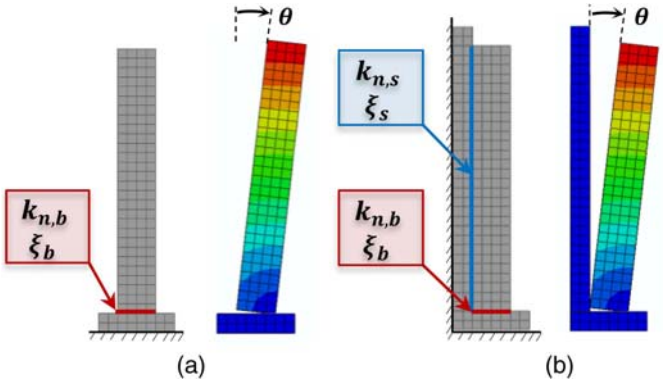

Fig. 5. Schematic representation of the numerical models adopted for (a) two-sided rocking motion; and (b) one-sided rocking motion.

numerical models is depicted in Fig. 5. Within ABAQUS CAE, the explicit solution scheme is adopted instead of an implicit scheme because it is preferable to proceed with the solution over small time increments. The main reason behind this choice is the reduced computational cost that the explicit scheme offers. Moreover, the contacting bodies of the problem are only forced to interact when they come into contact. The normal behavior of the contact area follows a linear stiffness pressure-overclosure relationship (i.e., soft contact approach). The tangential behavior adopts a penalty friction formulation with elastic stiffness and a friction coefficient that defines the slipping criterion. An artificially high value is given to the friction coefficient to avoid possible sliding at the contact interface, and dilatancy effects are neglected. For the case of the one-sided rocking problem of Fig. 5(b), distinct contact properties are set to govern the different body interactions, i.e., contact with the base ($k_{n,b}$) and with the sidewall ($k_{n,s}$). Finally, a viscous damping ratio ξ is directly assigned to the contact interfaces following the unilateral dashpot definition discussed previously, i.e., ξ_b at the base and ξ_s at the sidewall.

Fig. 6 shows the response of the analytical and numerical models through a series of free-rocking simulations for both two-sided [Figs. 6(a and b)] and one-side [Figs. 6(c and d)] rocking motions. Fig. 6 compares the two modeling approaches in terms of the rocking response history [Figs. 6(a and c)] and the total energy content expressed as the sum of the potential and kinetic energies of the system [Figs. 6(b and d)]. In Fig. 6, the initial rotation of the block is set to $\theta_0/\alpha = 0.5$, and the block has height $2h = 4.2$ m and base width $2b = 0.6$ m. For the analytical model, the COR that characterizes impact with the base is taken as $e_{2s} = 0.97$ [Eq. (3)], and the additional impact with the transversal wall, for the case of one-sided rocking, is captured through the $e_{tr} = -0.47$ [Eq. (4)]. For the numerical model, the damping ratio at the base is considered $\xi_b = 5.3\%$ [based on Eq. (11)], whereas for the one-sided rocking case, the damping ratio during contact with the sidewall is $\xi_s = 0.74\%$ [based on Eq. (13)].

Fig. 6 reveals the remarkable agreement between the two modeling approaches. Observe that only for lower rocking amplitudes and only for the two-sided rocking case [Figs. 6(a and b)] do the two examined models differ, with the numerical model dissipating energy slightly faster than the analytical model. Most importantly, from Figs. 6(b and d), the numerical (viscous damping) model shows a similar behavior with the analytical model, i.e., negligible energy loss during the smooth rocking motion phase, whereas step-like energy loss appears at each impact due to the unilateral dashpot formulation adopted herein. At the same time, the finite amount of energy dissipation at each impact is controlled by the damping ratio ξ. Therefore, by adjusting the damping ratio of the viscous damping model, energy equivalence between the two modeling approaches can be achieved. To this end, a calibration methodology is presented in the next section, with the aim of providing generalized predictive ξ–e relationships applicable to a variety of block-based (numerically simulated) structures that undergo either one-sided or two-sided rocking motion.

Importantly, even though the proposed numerical viscous damping model is presented using ABAQUS CAE, its applicability is universal and extended in other commonly used software for the numerical analysis of block-based rocking models. Fig. 7 presents a comparative investigation on the response of the rocking block of Fig. 5(a) derived by two additional commonly used block-based software, DIANA FEA version 10.4 (DIANA 2017), and 3DEC version 7.0 (Itasca 2013) through free-rocking simulations.

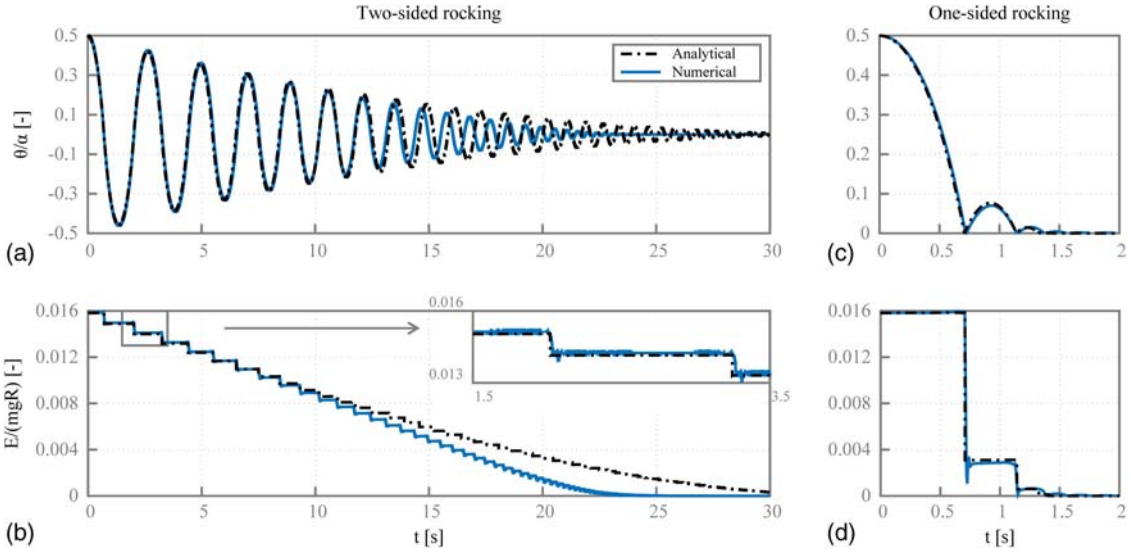

Fig. 6. Behaviour of the viscous damping model for (a and b) two-sided; and (c and d) one-sided rocking problems of Figs. 1 and 5. Comparison with the analytical model are conducted in terms of rocking angle in plots (a) and (c) and total energy content in plots (b) and (d). Details of the examined structure are $2h = 4.2$ m, $2b = 0.6$ m, $e_{2s} = 0.97$, $e_{tr} = -0.47$, $k_{n,b} = 5 \times 10^8$ N/m^3, $\xi_b = 5.3\%$, $k_{n,s} = 5 \times 10^8$ N/m^3, and $\xi_s = 0.74\%$.

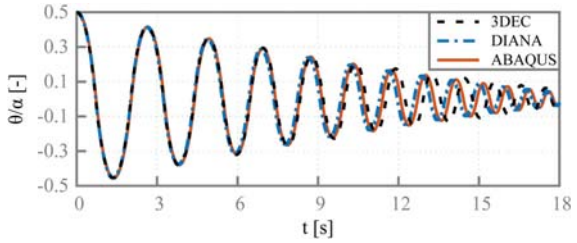

Fig. 7. Free-rocking response of the structure of Fig. 1(a) through three different numerical simulation software, i.e., ABAQUS CAE, DIANA FEA, and 3DEC. Details of the examined structure are $2h = 4.2$ m, $2b = 0.6$ m, $k_{n,b} = 5 \times 10^8$ N/m^3, and $\xi_b = 5.3\%$.

The three examined packages of modeling software are fundamentally different; however, the responses predicted by the adopted software are in almost excellent agreement. In particular, DIANA FEA adopts an implicit scheme to solve dynamic problems (compared with the explicit scheme adopted in ABAQUS CAE). Even though implicit schemes allow the use of larger time steps, the relatively high frequency at impact [Eq. (7)] imposes a strict upper limit to the adopted time step. At the same time, even if this restriction is disregarded, to control spurious high-frequency oscillations, artificial numerical dissipation is introduced, e.g., through the use of the Hilbert-Hughes-Taylor (HHT) algorithm (Hilber et al. 1977). Thus, relatively small time steps are eventually used in order for the viscous dissipation to dominate the artificial one.

To treat contact, DIANA FEA uses a zero-thickness interface element formulation, characterized by an elastic normal and tangential stiffness. The constitutive model of the interface is based on plasticity, following a nonassociative flow rule (with zero dilatancy) and a classical Mohr-Coulomb failure criterion. The physical damping is assigned to the interface elements based on a Rayleigh definition input. Because a unilateral SDR viscous damping is of interest, the alpha factor is set to zero and the beta factor is assigned accordingly to provide the desired ξ value at the $f_{\text{rot-contact}}$ of Eq. (7).

The software 3DEC, on the other hand, adopts an explicit solution scheme, which makes use of a central-difference algorithm to solve the equations of motion (Lemos 2019). This software is based on the discrete-element method whereby the structure is modeled as an assembly of discrete rigid or deformable blocks. Rigid blocks are used in this paper, as a result of which system deformability is assumed to be entirely concentrated at the interfaces between blocks. Contact between blocks is modeled using zero-thickness nonlinear interface springs (point contacts); thus, no joint or interface elements are defined. As in the case of ABAQUS CAE and DIANA FEA, the soft contact approach is also used here, with the extent of interpenetration between blocks being controlled by the interface stiffness, and the nonlinear response is controlled via the tensile strength in the normal direction (set to zero herein) and the Coulomb-slip joint model in the tangential direction, which depends in turn on the values specified for the cohesion (zero in this case) and the friction angle (set artificially high) (Pulatsu et al. 2019). Finally, stiffness proportional damping is used, which is specified through the damping ratio ξ and the frequency (in this case, $f_{\text{rot-contact}}$) at which it acts.

Fig. 7 illustrates a good agreement among the three simulation methodologies despite being fundamentally different (as explained previously). This conclusion highlights the universal applicability of the proposed numerical viscous damping model. The models used are readily available within each software package, and no additional implementations are required to reproduce the current results.

Proposed Numerical Model

Calibration Methodology

This section utilizes a calibration methodology of the proposed viscous damping model to achieve energy loss equivalence between the analytical model, based on the classical rocking theory of Housner (1963), and the numerical viscous damping model proposed in the previous section. Specifically, a phenomenological calibration methodology is adopted. To this end, free-rocking simulations are performed, where the analytical model is considered as a reference and the numerical (viscous damping) model is properly adjusted to fit it.

For the analytical model, the COR e (i.e., e_{2s} and e_{tr} for two- and one-sided rocking behavior, respectively) is assumed as an independent parameter. The choice to keep e independent of the geometry facilitates any correction to the assumptions of the classical rocking theory. Specifically, the COR e [e.g., in Eq. (11) and/or Eq. (13)] can be replaced by either an experimental correction ratio (Costa et al. 2013; Sorrentino et al. 2011; Tomassetti et al. 2019), or any theoretically refined model (Kalliontzis et al. 2016; Ther and Kollar 2017). Thus, the present approach allows the final calibrated relationship to be easily adapted to any existing or new experimental and theoretical refinement of the classical rocking theory.

For the numerical model, the damping ratio ξ (i.e., ξ_b and ξ_s for two- and one-sided rocking behavior, respectively) is considered the one that minimizes the root-mean square error (RMSE) metric

$$\text{RMSE} = \sqrt{\frac{1}{N} \cdot \sum_{t=1}^{N} (\theta_{an,t} - \theta_{\text{num},t})^2} \tag{9}$$

where $\theta_{an,t}$ = rocking rotation of the reference analytical model; $\theta_{\text{num},t}$ = rocking rotation of the numerical (viscous damping) model; t = sampling step; and N = total number of steps examined.

A sampling step of 0.01 s is considered adequately small for the two-sided rocking problem [Figs. 1(a) and 5(a)] because the whole response-history lasts for several seconds [Fig. 6(a)]. On the contrary, because the one-sided rocking problem [Figs 1(b) and 5(b)] experiences a fast decay after impacts [Fig. 6(c)], a sampling step of 0.001 s is preferred. The total number of steps is selected in each case up to the point where the response has experienced a relative decay ratio $r = \theta_t/\theta_0$ of 95% for the two-sided and 99.95% for the one-sided case, respectively, i.e., $\forall t$, until $\exists\ \theta_t \geq (1-r)\theta_0$.

Before conducting the calibration for each rocking problem (i.e., two-sided and one-sided rocking), the influence of the different parameters involved needs to be examined. In other words, only the most critical independent parameters will be retained during the calibration process. Table 2 presents the parameters to be investigated for each rocking problem and the corresponding range of values. These parameters include the slenderness (or aspect ratio) of the block (h/b), the scale of the block (R), the rocking amplitude (θ_0/α), and the normal interface stiffness (k_n), as defined in the previous sections. Both the reference and range of values in Table 2 have been chosen to be representative of unreinforced masonry structures (Derakhshan et al. 2013; Doherty et al. 2002; Tomassetti et al. 2019). However, due to the wide range of the examined parameters, the calibrated ξ–e expressions can also be applicable to various rocking structures that can be dynamically equivalent to block-based structures and whose parameters fall within the

Table 2. Independent parameters examined for the calibration process (Fig. 8) of the two-sided and one-sided rocking

Parameter	Range	Reference value
Scale, R (m)	1.4–2.8	2.1
Slenderness, h/b	4.0–15.0	7.0
Amplitude, θ_0/α	0.3–0.8	0.5
Normal interface stiffness at base, $k_{n,b}$ (N/m^3)	0.5×10^8–30×10^8	5×10^8
Normal interface stiffness at side, $k_{n,s}$[a] (N/m^3)	0.5×10^8–30×10^8	5×10^8

[a]Only for the one-sided rocking case.

examined range. An overview flowchart of the calibration methodology is shown in Fig. 8, indicating the key steps of the process.

Recall that the classical rocking theory (Housner 1963) assumes that energy loss (captured through the COR) depends only on the slenderness of the block α [Eqs. (3) and (4)]. Therefore, the scale (R) and amplitude (θ_0/α) do not affect the energy loss process. At the same time, the rigidity of the structure–foundation interaction assumed in the classical rocking theory excludes the influence of the interface stiffness from the energy dissipation process. To this end, the analytical model adopted herein as reference is in accordance with the classical rocking theory and disregards any influence of the normal interface stiffness at the base ($k_{n,b}$) and/or the sidewall ($k_{n,s}$). However, recent experimental tests revealed that the interface stiffness affects the rocking response. In particular, ElGawady et al. (2011) and Spanos et al. (2017) highlighted that blocks rocking on a flexible foundation usually experience higher energy loss than that of the classical rocking theory. Nevertheless, the experimental rocking response can be statistically captured by the classical rocking theory (Bachmann et al. 2018), as long as the rigid block assumption is adequately respected (which is reasonable for masonry structures where monolithic behavior can be ensured). Hence, the numerical model adopts a material elasticity modulus of 50 GPa. Such a value, representative of, e.g., hard granite material, is considered high enough to ensure that the block's deformation is negligible compared with the interface. A thorough investigation of the interaction of block's flexibility with its rocking response merits further investigation and is beyond the scope of the present study; however, it will be addressed in detail in future work.

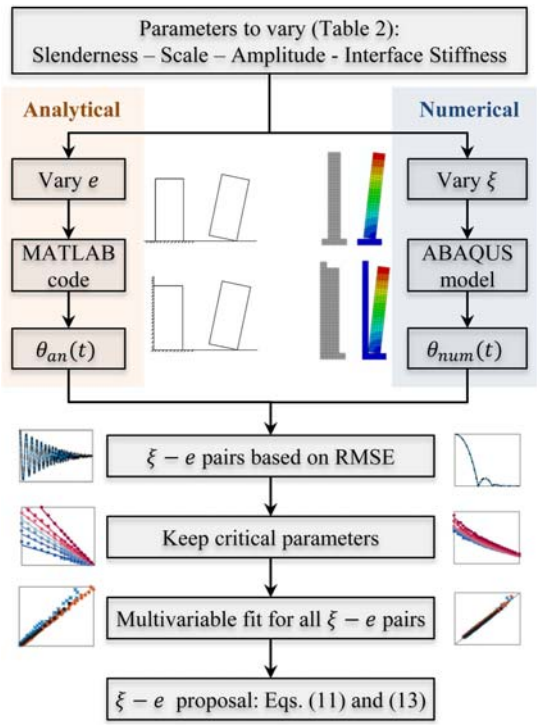

Fig. 8. Flowchart of the adopted phenomenological calibration process.

Two-Sided Rocking Motion

This section applies the calibration methodology illustrated in Fig. 8 and proposes a novel ξ_b–e_{2s} relationship that captures the response history of any block-based numerical model that undergoes two-sided rocking motion [e.g., Figs. 1(a) and 5(a)]. As a first approach, the influence on the response of the main parameters involved in the problem, i.e., scale (R), slenderness (or aspect ratio) (h/b), rocking amplitude (θ_0/α), and normal interface stiffness at the base ($k_{n,b}$), are studied independently. For each combination of the examined parameters, as the COR e_{2s} varies, a unique ξ_b is determined that minimizes the RMSE error metric [Eq. (9)]. Fig. 9 plots those ξ_b–e_{2s} pairs identified with a unique point marker and reveals the influence of each independent parameter examined herein. For each combination, a logarithmic function is fitted to these points, having the form (Makris and Konstantinidis 2003; Tomassetti et al. 2019)

$$\xi_b = c \cdot \ln e_{2s} \tag{10}$$

where c = constant computed by the fitting process.

Fig. 9 plots also the fitted functions identified with solid lines. Fig. 9 reveals that the logarithmic function of Eq. (10) provides a good estimation of the ξ_b–e_{2s} correlation, at least for the specific range of values examined in Table 2.

Fig. 9(a) presents the results of three different scales R (Table 2). Importantly, Fig. 9(a) unveils that the scale does not influence the performance of the numerical (viscous damping) model. Therefore, it can be disregarded from the two-sided rocking calibration process (thus, the reference value of $R = 2.1$ m is considered for the rest of the calibration process).

On the contrary, a significant influence is noticed when the slenderness (or aspect ratio) h/b is varied, as illustrated by Fig. 9(b). More specifically, Fig. 9(b) reveals that the more slender the structure, the higher the damping ratio required by the numerical model to dissipate an equal amount of energy compared with the analytical model. Interestingly, such a trend is in agreement with the classical rocking theory (Housner 1963), which suggested that stockier rocking blocks experience higher energy dissipation than more slender ones.

Fig. 9(c) investigates the effect of the rocking amplitude on the numerical (viscous damping) model. Compared with the influence of the other independent parameters, the influence of the amplitude θ_0/α is considered marginal. In addition, including this dependency would significantly complicate the calibration process because the rocking amplitude is unknown a priori to any forced-vibration analysis. Therefore, the median rocking amplitude of $\theta_0/\alpha = 0.5$ is used for the rest of the calibration process. This choice is expected to be on the engineering safe side (i.e., on the conservative side, by dissipating less energy than dictated) for the large and critical oscillations, whereas higher energy loss is anticipated in low rocking amplitudes [Fig. 6(a)]. The implications of this choice are discussed in more detail subsequently.

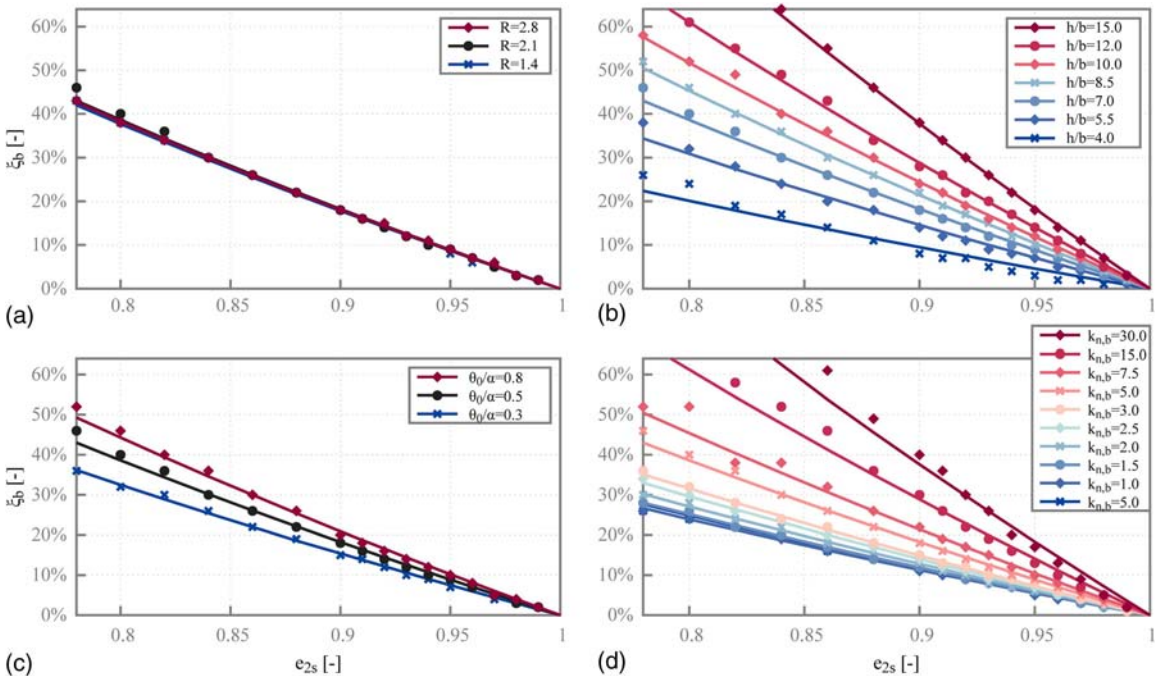

Fig. 9. Influence of (a) scale R; (b) slenderness (or aspect ratio) h/b; (c) amplitude θ_0/α; and (d) interface stiffness $k_{n,b}$ at the base on the response history of the block of Figs. 1(a) and 5(a) when it undergoes two-sided rocking motion.

Finally, Fig. 9(d) suggests a high sensitivity of the viscous damping model to the normal interface stiffness at the base $k_{n,b}$. A model with lower stiffness appears to inherently dissipate more energy for a given damping ratio. Thus, it requires a lower damping ratio ξ to efficiently capture the analytical rocking response. This trend is in line with the experimental findings of ElGawady et al. (2011) and Spanos et al. (2017), where blocks rocking on flexible foundations (e.g., of rubber-type material) were observed to dissipate more energy than when they rock on less flexible foundations (e.g., marble or concrete). Nevertheless, as discussed in the previous section, because this influence has not yet been quantified in the literature, the normal interface stiffness is treated as an additional independent parameter during the ξ_b–e_{2s} calibration process.

To summarize, Fig. 9 shows that the slenderness (or aspect ratio) h/b and normal interface stiffness at the base $k_{n,b}$ are the most critical parameters that influence the energy dissipation during the whole response history of the two-sided rocking problem [Fig. 5(a)]. Hence, after conducting multivariable nonlinear regression analysis on the results of Fig. 9, the novel ξ_b–e_{2s} relationship that connects the damping ratio of any block-based numerical model with the COR e_{2s} is expressed

$$\xi_b = -0.000292 \cdot \left(\frac{H}{B}\right)^{0.935} \cdot k_{n,b}^{0.343} \cdot \ln e_{2s} \qquad (11)$$

The adequacy of the proposed ξ_b–e_{2s} relationship of Eq. (11) to predict the measured ξ_b is visualized in Fig. 10. A coefficient of determination of $R^2 = 0.978$ characterizes all the data points, indicating a remarkable estimation capability of the proposed ξ_b–e_{2s} relationship [Eq. (11)]. In more detail, whereas the slenderness variation appears to capture the measured ξ_b quite well, with all points lying close to the reference line, the stiffness variation shows a slightly higher discrepancy, yet with the tendency to underestimate the damping ratio, thus giving a response on the conservative side.

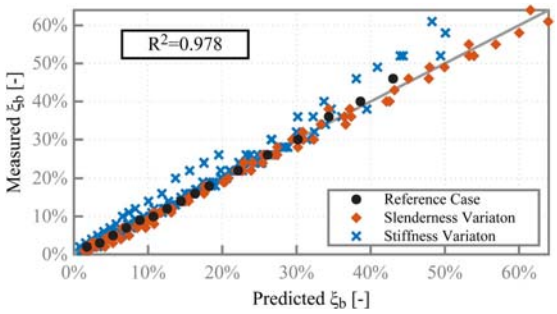

Fig. 10. Predicted versus measured plot given by the ξ_b–e_{2s} relationship of Eq. (11).

One-Sided Rocking Motion

This section focuses on the one-sided rocking problem of Figs. 1(b) and 5(b) and offers a novel ξ_s–e_{tr} relationship which, together with Eq. (11), captures the response history of any block-based numerical model that undergoes one-sided rocking motion. From an analytical perspective, the one-sided rocking problem can be analyzed assuming two distinct CORs [Eq. (5)]: (1) e_{2s} to capture the energy dissipation for impacts against the base, and (2) e_{tr} for impacts against the transversal wall [Fig. 1(b)]. Numerically, the impacting/contacting areas are governed by distinct contact/interface properties [Fig. 5(b)]: $k_{n,b}$ and ξ_b for normal interface stiffness and damping ratio at the base, and $k_{n,s}$ and ξ_s for normal interface stiffness and damping ratio at the side (i.e., the transversal wall), respectively. Therefore, the expression between ξ_b–e_{2s} of Eq. (11) is directly applied at the base, and the ξ_s–e_{tr} relationship is investigated. Similarly, the scale (R), slenderness (or aspect ratio) (h/b), rocking amplitude (θ_0/α), normal interface stiffness at the base ($k_{n,b}$), and the normal interface stiffness at the side ($k_{n,s}$) are considered as the independent parameters, and their influence on the

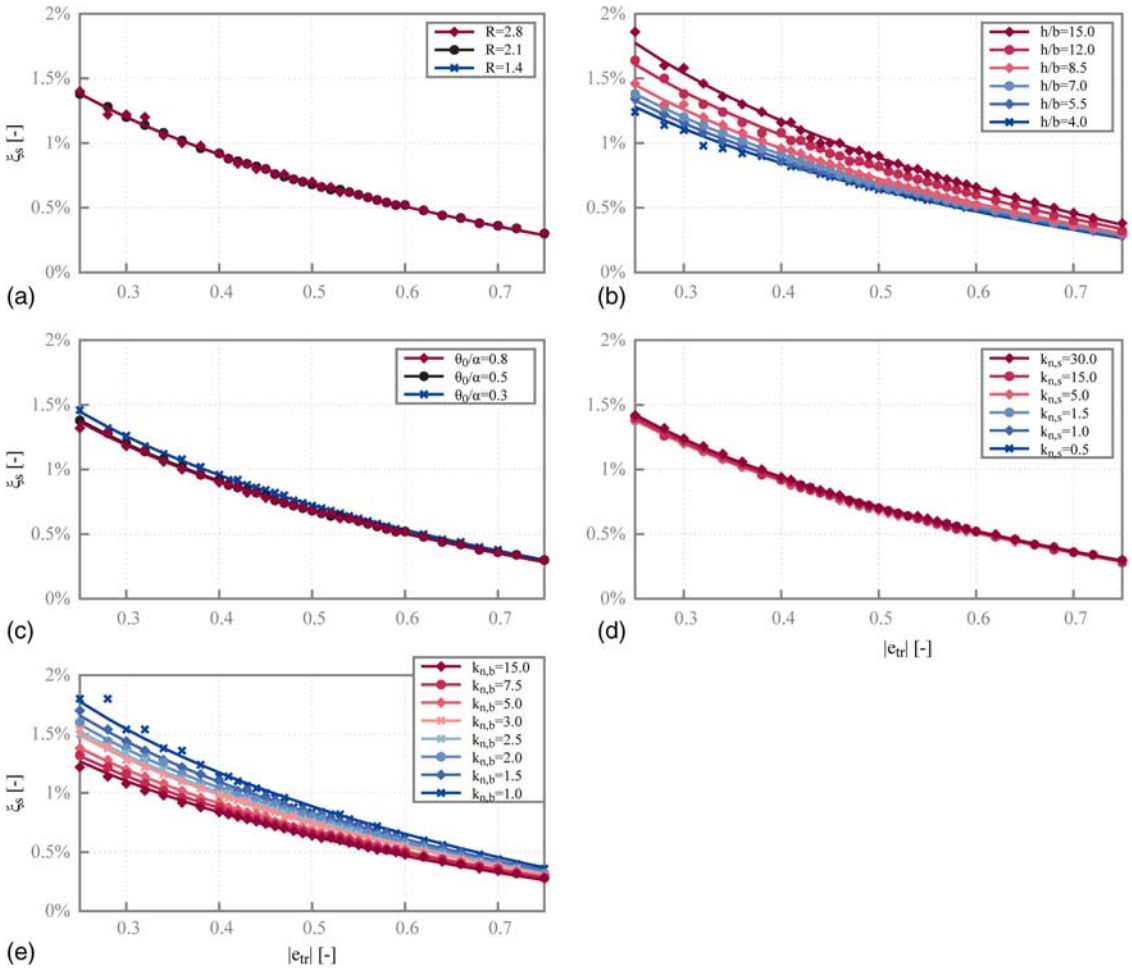

Fig. 11. Influence of (a) scale R; (b) slenderness (or aspect ratio) h/b; (c) amplitude θ_0/α; (d) interface stiffness $k_{n,s}$ at the side; and (e) interface stiffness $k_{n,b}$ at the base on the response history of the block of Figs. 1(b) and 5(b) when it undergoes one-sided rocking motion.

whole response-history of the numerical model are examined herein.

Fig. 11 plots the e_{tr}–ξ_s pairs that minimize the RMSE error metric [Eq. (9)]. Similar to the two-sided rocking problem, a logarithmic function of the following form is fitted on each combination

$$\xi_s = d \cdot \ln|e_{tr}| \tag{12}$$

where d = constant computed by the fitting process. Fig. 11 presents also the fitting functions identified as solid lines. Again, Fig. 11, the adopted logarithmic function of Eq. (12) satisfactorily fits the ξ_s–e_{tr} variation for all combinations.

Fig. 11(a) illustrates the influence of the scale R, and it shows that, as in the case of two-sided rocking [Fig. 9(a)], the viscous damping model is not affected by the scale variation. Thus, the influence of the scale is disregarded from the one-sided rocking calibration process (using as a reference the value of $R = 2.1$ m for the rest of the calibration process).

Conversely, varying the slenderness (or aspect ratio) h/b appears to have a significant influence on the response given by the numerical model [Fig. 11(b)]. Specifically, more slender rocking blocks suggest the use of a higher damping ratio in order to ensure the same energy dissipation (i.e., equal COR e_{tr}) as the analytical model. Similarly, this trend follows the theoretical indication that slender rocking blocks dissipate less energy than stockier blocks.

Fig. 11(c) investigates the effect of the rocking amplitude θ_0/α on the numerical (viscous damping) model. It shows that the influence is almost negligible, especially when compared with the pertinent influence of the other parameters, i.e., slenderness h/b [Fig. 11(b)] and/or normal interface stiffness at the base $k_{n,b}$ [Fig. 11(e)]. Therefore, the rocking amplitude can be omitted for the rest of the calibration process, with the median value of $\theta_0/\alpha = 0.5$ to be considered for the rest of the calibration process.

In addition, Figs. 11(d and e) illustrate the role of the normal interface stiffness at the side and the base, respectively. Specifically, Fig. 11(d) shows that the normal interface stiffness at the side $k_{n,s}$ does not influence the performance of the viscous damping model. On the contrary, the normal interface stiffness at the base $k_{n,b}$ significantly affects the performance of the viscous damping model. Therefore, only the latter is included in the calibration process (using as a reference value $k_{n,s} = 5 \times 10^8$ N/m^3 for the rest of the calibration process).

To summarize, Fig. 11 shows that the slenderness (or aspect ratio) h/b and the normal interface stiffness $k_{n,b}$ at the base are the most critical independent parameters that influence the energy dissipation during the whole response history of the one-sided rocking problem [Figs. 1(b) and 5(b)]. Similarly, following a multivariable nonlinear regression analysis on the results of Fig. 11, the novel ξ_s–e_{tr} relationship is expressed

$$\xi_s = -0.0807 \cdot \left(\frac{H}{B}\right)^{0.2548} \cdot k_{n,b}^{-0.1283} \cdot \ln|e_{tr}| \tag{13}$$

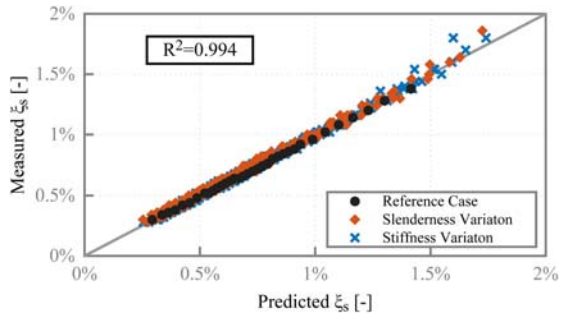

Fig. 12. Predicted versus measured plot given by the ξ_s–e_{tr} relationship of Eq. (13).

Fig. 12 assesses the accuracy of the proposed relationship of Eq. (13) through a predicted-versus-measured plot. Fig. 12 reveals the excellent estimation capability of the proposed ξ_s–e_{tr} relationship of Eq. (13), which translates into a coefficient of determination of $R^2 = 0.994$.

Performance Evaluation of the Proposed Numerical Model

To assess the reliability of the proposed numerical viscous damping model, a validation process is crucial. This section compares the proposed numerical model with experimental results from the literature. In particular, three experimental campaigns investigating both two-sided (Peña et al. 2008) and one-sided rocking motion (Al Shawa et al. 2012; Sorrentino et al. 2011) are adopted as reference for the proposed numerical model. Both rocking problems are tested initially against free-rocking experiments, where the importance of energy loss is more profound. For a more holistic validation, the proposed numerical model is also evaluated against forced-rocking tests. Merits and shortcomings of the proposed numerical model are highlighted in the following sections.

Validation against Two-Sided Free- and Forced-Rocking Tests

A comprehensive experimental campaign of rocking granite blocks has been conducted by Peña et al. (2008). The two-sided free- and forced-rocking motion of three specimens presented by Peña et al. (2008) are adopted to validate the proposed numerical (viscous damping) model. Table 3 provides the structural characteristics of the examined specimens. Peña et al. (2008) calculated an experimental COR (Table 3), which is slightly higher than the theoretical proposal [Eq. (3)]. Therefore, to avoid biased conclusions, the experimentally calculated COR is adopted here as input for the viscous damping model of Eq. (11), thus, illustrating its ability to be adapted to refined and/or experimentally measured COR proposals.

In addition to the classical material parameters, numerical modeling requires the use of a normal interface stiffness. However, this parameter was not measured experimentally by Peña et al. (2008). Thus, an estimated value for the normal interface stiffness at the base $k_{n,b} = 5 \times 10^8$ N/m^3 is adopted herein, which falls within the range of values adopted in previously conducted investigations on rocking masonry walls and could be considered representative of moderately stiff foundations. However, to facilitate the better understanding of the interface stiffness $k_{n,b}$ on the overall energy dissipation, additional $k_{n,b}$ values (i.e., 1×10^8 and 10×10^8 N/m^3) are also examined and plotted in Fig. 13.

As a first approach, the free-rocking response of the three specimens is examined in Figs. 13(a–c). Figs. 13(a–c) show that, in general, the proposed viscous damping model is able to reproduce relatively well the overall dissipation phenomena of the different specimens. Even when varying the interface stiffness $k_{n,b}$, the overall response-history follows a similar response envelope despite varying slightly in phase. Specifically, for some cases, alternative $k_{n,b}$ values might capture the phase of the response slightly better [e.g., Fig. 13(a)] or worse [e.g., Fig. 13(b)] than the reference value of 5×10^8 N/m^3 without affecting the peak response. However, to avoid confusion, the value of $k_{n,b} = 5 \times 10^8$ N/m^3 is considered for the remaining part of this study. Results of Figs. 13(a–c) can be further appreciated if one also considers that the different specimens are characterized by different values of slenderness and thus different CORs [Eq. (3)] which can significantly influence the response.

However, the proposed numerical model behaves in a robust way, adequately capturing the whole response history. In particular, the rocking motion of Specimen 1 [Fig. 13(a)] with an experimentally measured $e_{2s} = 0.936$ damps out after approximately 3 s, whereas the numerical model damps out after around 2.5 s. For Specimens 2 [Fig. 13(b)] and 3 [Fig. 13(c)] with experimentally measured $e_{2s} = 0.973$ and $e_{2s} = 0.978$, the rocking response lasts approximately 13 and 14 s, respectively, whereas the numerical reproduction indicates a response of 13 s in both cases. Nevertheless, it is also clear from Figs. 13(a–c) that for Specimens 1 and 3 the numerical damping model dissipates energy faster than the experiments. More specifically, a very good agreement is achieved in the first cycles of response. However, for smaller rocking angles, the two response-histories start diverging. This shortcoming of the damping model (i.e., to dissipate more energy at lower amplitudes) is anticipated already by the calibration process. Specifically for the two-sided rocking problem, Fig. 9(c) highlights the dependency of dissipation on the rocking amplitude. Given this amplitude sensitivity, one could suggest its inclusion in the damping proposal [Eq. (11)] to better capture the complete response decay. However, this would not be of practical interest because the rocking amplitude is unknown a priori in the case of random ground excitations. Regardless of that limitation, the viscous damping model proposed in Eq. (11) performs quite well for rocking amplitudes $0.3 < \theta_0/\alpha < 0.8$, whereas for higher or lower amplitudes, less and more dissipation is expected, respectively. Ideally, a damping

Table 3. Details of the adopted specimens and examined tests of Peña et al. (2008)

Specimen	$2h$ (m)	$2b$ (m)	$e_{2s,\text{exp}}$	ξ_b (%)	Tests examined
1	1.0	0.25	0.936	6.79	(1) Free-rocking; and (2) harmonic sinusoidal excitation with $f = 3.3$ Hz, $a_p = 6$ mm, and $t = 20$ s
2	1.0	0.17	0.973	4.03	(1) Free-rocking; and (2) harmonic sinusoidal excitation with $f = 5$ Hz, $a_p = 5$ mm, and $t = 10$ s
3	1.0	0.12	0.978	4.53	(1) Free-rocking; and (2) synthetic ground excitation records: 18, load factor: 0.5 [Peña et al. (2008) give more details]

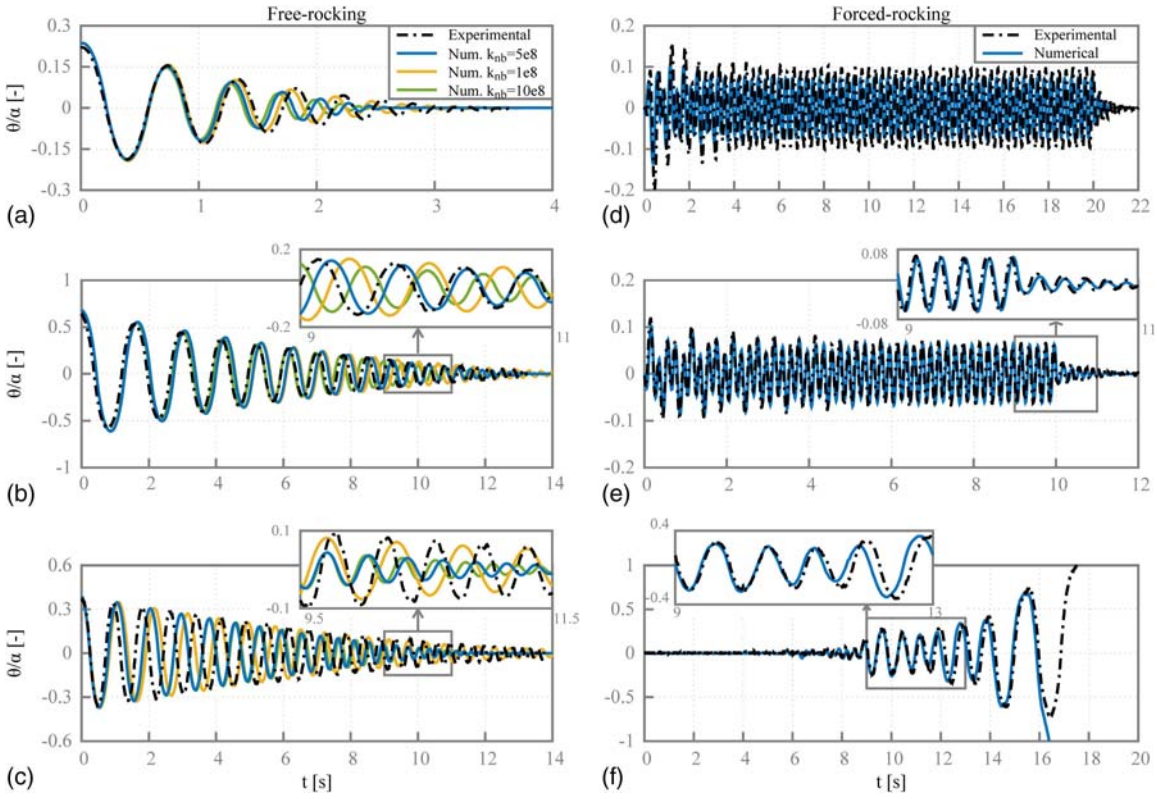

Fig. 13. (a–c) Two-sided free-rocking response; and (d–f) forced-rocking response of the proposed numerical (viscous damping) model compared with the experimental response reported by Peña et al. (2008) of (a) Specimen 1 under free rocking; (b) Specimen 2 under free rocking; (c) Specimen 3 under free rocking; (d) Specimen 1 under harmonic sinusoidal excitation; (e) Specimen 2 under harmonic sinusoidal excitation; and (f) Specimen 3 under a synthetic ground excitation (Table 3).

model that adapts ad hoc depending on the motion's amplitude could tackle the issue. This issue, however, merits further investigation because such an attribute is not readily available in commonly used viscous damping models and it is beyond the scope of the present study.

The performance of the numerical (viscous damping) model is also evaluated against forced vibration tests (Peña et al. 2008) in Figs. 13(d–f). More specifically, Specimens 1 [Fig. 13(d)] and 2 [Fig. 13(e)] are subjected to harmonic sinusoidal excitations with different characteristics, and Specimen 3 [Fig. 13(f)] is subjected to a synthetic earthquake excitation (Table 3). Figs. 13(d–f) reveal the remarkable agreement of the proposed numerical model with the experimental results reported by Peña et al. (2008). More specifically, the numerical model effectively replicates the different phases of the experimental response-history, i.e., the transient, stationary, and free decay phase. Only when the rocking block reaches high rocking amplitudes critical to its stability (i.e., $\theta_0/\alpha > 0.8$) does the proposed numerical model overpredict the rocking response resulting in earlier collapse [Fig. 13(f)]. Overall, the numerical model is capable of capturing the experimental response with adequate accuracy, particularly with respect to the phase of oscillations, peak response, and potential overturning.

Validation against One-Sided Free- and Forced-Rocking Tests

This section evaluates the proposed numerical viscous damping model against one-sided free- and forced-rocking experimental tests. To that end, this work adopts the experimental campaign of Sorrentino et al. (2011) for the one-sided free-rocking simulations and the tests conducted by Al Shawa et al. (2012) for the one-sided forced-rocking evaluation.

In terms of one-sided free-rocking tests, a variety of geometrical configurations, materials, and boundary conditions were tested by Sorrentino et al. (2011). Table 4 presents the cases adopted herein together with their structural characteristics to test the performance

Table 4. Details of the examined one-sided free-rocking tests of Sorrentino et al. (2011)

Reference code	H (m)	$\alpha_{\text{inst,exp}}$ (rad)	$e_{1s,\text{exp}}$	$e_{2s,an}$	$e_{tr,\text{exp}}$	ξ_b (%)	ξ_s (%)
brick, h80, cd12, t01	0.8	0.1184	−0.328	0.979	−0.342	4.35	1.15
brick, h82, cd06, t03	0.82	0.1157	−0.441	0.980	−0.460	4.24	0.84
brick, h136, cd06, t01	1.36	0.0420	−0.458	0.997	−0.461	1.44	1.09
brick, h163, cd06, t01	1.63	0.0371	−0.273	0.998	−0.274	1.26	1.87
tuff, h128, cd12, t02	1.28	0.0699	−0.403	0.993	−0.409	2.48	1.10
tuff, h163, cd12, t02	1.63	0.0546	−0.309	0.995	−0.312	1.90	1.52

Note: Reference code = material, height (cm), contact depth of sidewalls, test number.

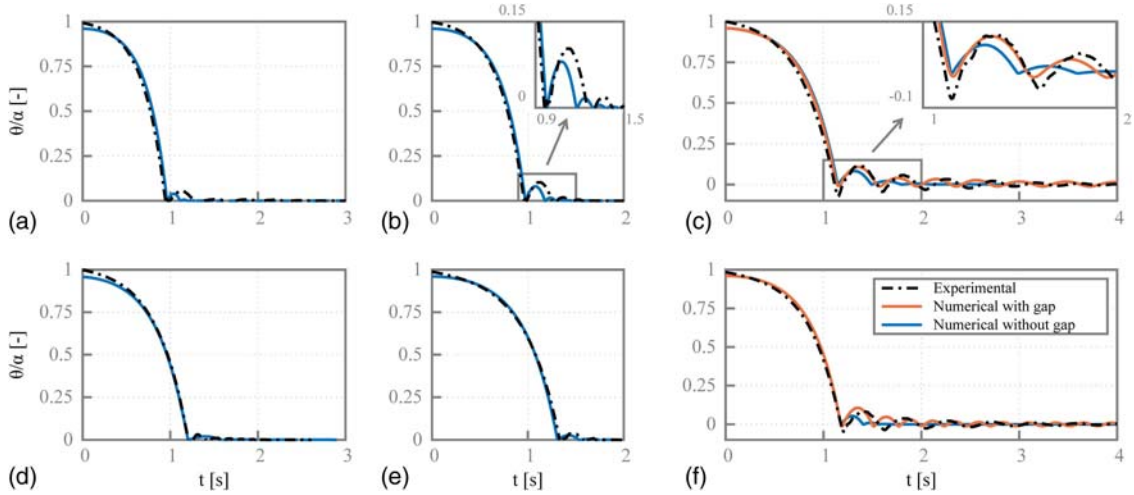

Fig. 14. One-sided free-rocking response of the proposed numerical (viscous damping) model compared with the experimental response reported by Sorrentino et al. (2011): (a) brick, h80, cd12, t01; (b) brick, h82, cd06, t03; (c) brick, h136, cd06, t01; (d) brick, h163, cd06, t01; (e) tuff, h163, cd12, t02; and (f) tuff, h128, cd12, t02 (Table 4).

of the proposed viscous damping model. In Table 4, $\alpha_{\text{inst,exp}}$ denotes the rocking angle at which the free rocking initiates (Sorrentino et al. 2011), and $e_{1s,\text{exp}}$ is the experimentally measured (total) COR [equivalent to the COR of Eq. (5)]. Subsequently, the COR that characterizes solely the impact with the transversal wall $e_{tr,\text{exp}}$ can be analytically calculated using Eq. (5), i.e., $e_{tr,\text{exp}} = e_{1s,\text{exp}}/(e_{2s,an})^2$ where $e_{2s,an}$ is given by Eq. (3) using $\alpha_{\text{inst,exp}}$. At the same time, the impact with the base is characterized by the analytical value of the COR $e_{2s,an}$ of Eq. (3).

Similar to the previous subsection and due to the absence of data regarding the normal stiffness at the interfaces, this subsection assumes values of $k_{n,b} = 5 \times 10^8$ N/m^3 for the stiffness at the base and $k_{n,s} = 5 \times 10^7$ N/m^3 for the stiffness at the side. The stiffness at the side is assumed to be one order of magnitude lower than the stiffness at the base due to the absence of acting axial load at the vertical interface (e.g., Lourenço et al. 2005, among others). The corresponding damping ratios at the base and the side are then computed using Eqs. (11) and (13), respectively.

Fig. 14 plots the response-histories of the examined cases of Table 4. In general, Fig. 14 shows that the numerical (viscous damping) model can capture the experimental response quite well if, again, one considers that due to the universal behavior of the proposed numerical model a single value is adopted to characterize the interface stiffness at the base and the side, respectively. Also, the numerical (viscous damping) model fails to capture the initial rotation θ_0/α due to the way the experimental test was conducted (Sorrentino et al. 2011), which causes some discrepancies during the first cycle of rotation. In particular, the initial rotation is controlled by a mechanical system that prevents overturning of the specimen. In this way, it is possible to assign a limit value of the initial rotation (i.e., $\alpha_{\text{inst,exp}}$ in Table 4) at which the experimental free-rocking motion commences. However, that initial value of rotation causes overturning to the numerical model because it is too close to the instability rotation. Therefore, numerically, a slightly lower value of the initial rotation is assigned to ensure free-rocking motion without causing overturning.

In addition, observe from Fig. 14 that even though the experiments were designed without a gap between the specimen and the transversal walls, slight negative oscillations were observed [i.e., Figs. 14(c and f)]. Such negative oscillations might be a result of a presence of a gap due to e.g., debris accumulation and/or construction imperfections during the test, or a manifestation of the reduced effective base width of the masonry wall, and thus, inward-shifted pivoting. The experimental response is better captured when a gap between the rocking façade and the transversal wall is introduced in the numerical model [Figs. 14(c and f)]. This rather simple comparison highlights the sensitivity of the response of such tests, and, thus, explains small discrepancies between the experimental and numerical model.

Despite the aforementioned discrepancies coupled with the uncertainties regarding the CORs computed analytically and the appropriate value of the normal interface stiffness, it is clear that the overall dissipative phenomena are still very well captured by the numerical (viscous damping) model: significant amount of energy is lost at impact, resulting in the damping out of the oscillation after two or three impacts.

To further evaluate the proposed damping model against one-sided forced-rocking tests, this study adopts the experimental campaign of real-scale one-sided rocking tuff-masonry walls performed by Al Shawa et al. (2012). The façade tested has a width of $2b = 0.25$ m and height $2h = 3.0$ m. Specific details regarding the shaking table excitation input can be found in Table 5. Before each test reported by Al Shawa et al. (2012), an initial out-of-plumb rotation was measured (η/α in Table 5) due to the sequential testing and mortar debris accumulation within the cracked joint. Moreover, a small gap of 4 mm between the rocking façade and the transversal wall was also noticed (Al Shawa et al. 2012).

Furthermore, the normal interface stiffness at the base of the block is again assumed to be $k_{n,b} = 5 \times 10^8$ N/m^3, which according to Eq. (7) results in $f_{\text{contact}} = 2.5$ Hz, close to the experimentally measured frequencies prior to testing (i.e., around 1–2 Hz). This assumption considers zero influence of the transversal walls on the frequency of the rocking façade when at rest, which is reasonable given the initial out-of-plumb rotation. As in the case of the

Table 5. Details of the examined one-sided forced-rocking tests of Al Shawa et al. (2012)

TH	Record	SF	PGA (g)	PGV (cm/s)	η/α (%)	f (Hz)
22	R1168EW	0.42	0.145	9.0	3.7	1.1
31	R1168EW	0.70	0.309	15.2	5.7	1.1

Note: SF = scale factor; PGA = peak ground acceleration; and PGV = peak ground velocity.

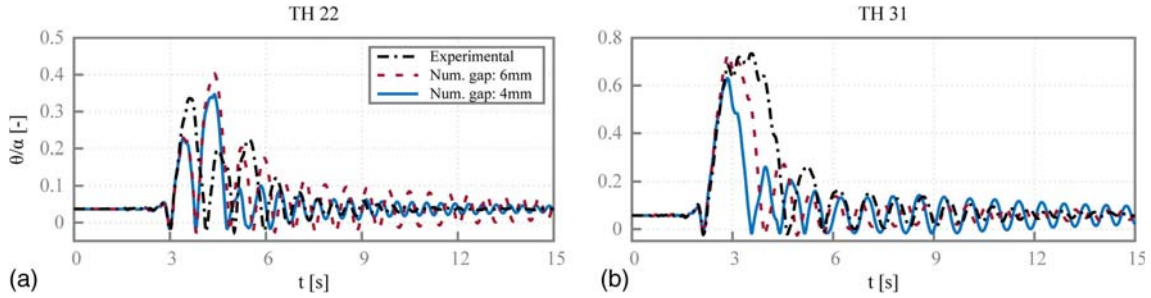

Fig. 15. One-sided forced-rocking response of the proposed numerical (viscous damping) model compared with the experimental response reported by Al Shawa et al. (2012) under (a) TH 22; and (b) TH 31.

free-rocking tests, the normal interface stiffness at the side is assumed to be $k_{n,s} = 5 \times 10^7$ N/m^3. Both COR values (e_{2s} and e_{tr}), and the pertinent damping ratios (ξ_b and ξ_s), required for these tests were computed by the analytical Eqs. (5) and (6) and the proposed Eqs. (11) and (13), respectively (i.e., $e_{2s} = 0.989$, $e_{tr} = -0.489$, $\xi_b = 2.98\%$, and $\xi_s = 0.84\%$).

Fig. 15 presents a comparison of the proposed numerical (viscous damping) model with experimental one-sided forced-rocking tests from Al Shawa et al. (2012). Tests 22 and 31 (i.e., TH 22 and TH 31 in Table 5) are examined in more detail here, as shown in Fig. 15. In the case of TH 22, Fig. 15(a) illustrates a good agreement between the prediction of the numerical model and the experimental response in terms of the peak response and amplitude decay for the assumed gap of 4 mm (based on Al Shawa et al. 2012). However, the numerical model fails to capture the phase of the experimental response. In contrast, Fig. 15(b) reveals a poor agreement in terms of both the amplitude and phase of oscillations for the dictated gap of 4 mm. The repetition of the test might have led to a progressive increase in the magnitude of the gap due to, e.g., debris accumulation. In this context, better agreement of the response is achieved in terms of both the peak response and amplitude decay when increasing the gap at the interface between the façade and the sidewall to 6 mm. This conclusion highlights the sensitivity of the response to specific characteristics of the experimental setup. Nevertheless, the proposed numerical (viscous damping) model shows adequate adaptability and robustness to such case-specific experimental characteristics.

Conclusions

This paper presented a novel viscous damping model that derives equivalence between the damping of numerical block-based models and the impulsive nature of energy loss of the classical rocking theory. Specifically, new predictive equations are proposed and calibrated through over 1,000 free-rocking numerical simulations, which correlate the damping ratio of the numerical model to the coefficient of restitution of the statistically accurate classical rocking theory, for both the two-sided and one-sided rocking cases. The former is representative of the behavior of structures such as parapet walls, which are free to rock in both positive and negative directions, with impact only against the base, whereas the latter is more commonly observed in the case of façades, which are generally free to rock in only one direction, with impact taking place against the base and transverse walls.

The performance of the new model is evaluated through comparisons with experimental tests from the literature. In general, the novel numerical model performs reasonably well for the two-sided free-rocking case, with only slightly faster energy dissipation than its experimental counterpart. The two response-histories are in very good agreement in terms of both phase and peak amplitudes for the first cycles of motion.

In the case of forced rocking, the numerical model is again able to reproduce the experimental response with good accuracy in terms of oscillation phase and peak response, as well as potential overturning. In fact, for rocking amplitudes in the range of 30% to 80% of the critical (overturning) rotation ($0.3 \leq \theta/\alpha \leq 0.8$), which is also the range of practical engineering interest, the response is adequately captured for both free- and forced-rocking motion. For higher amplitudes, the response is slightly underdamped, which, however, is on the engineering safe or more conservative side.

In the case of one-sided rocking, a fair comparison is again observed for the free-rocking case, with the numerical model once again damping out marginally faster than the experimental tests. Further, the sensitivity of the response to the gap at the interface between the structure and the sidewall is also highlighted. However, this work reveals how adequately well the proposed numerical model captures the experimental response despite the major influence of the gap (on the response). This is also emphasized through the forced-rocking simulations, where the assumed value of the gap is found to strongly influence the predictions of the numerical model. Nevertheless, the proposed numerical (viscous damping) model shows adequate adaptability and robustness to capture the peak amplitude (albeit with some differences in phase) as well as the overall decay of the rocking motion.

Importantly, although the numerical simulations presented in this paper have been conducted in ABAQUS CAE, the universality of the proposed viscous damping model enables it to be used in fundamentally different numerical simulation software used for the analysis of block-based rocking models (i.e., DIANA FEA and 3DEC)—thus highlighting its broad applicability.

In conclusion, this work offers reliable and ready-to-use expressions that capture the energy loss mechanism of any block-based numerical model that undergoes either one-sided or two-sided planar rocking motion—in agreement with the well-established classical rocking theory. Importantly, the results of the present study serve as the basis for a more rational and holistic approach to model multi-degree-of-freedom rocking structures, the interaction of complex geometries and boundary conditions with the rocking response, and/or the inclusion of material nonlinearities, among others. Even though the proposed numerical (viscous damping) model was evaluated against the two most commonly observed out-of-plane collapse mechanisms of unreinforced masonry structures, to further enhance its applicability, a more thorough investigation against additional collapse mechanisms (e.g., vertical spanning strip wall or the corner mechanism) is required. Such analyses, however, should be accompanied by extensive experimental campaigns,

which are currently lacking in the literature and thus are topics of future research.

Data Availability Statement

Data used during the study were provided by third parties, i.e., the experimental data used for the purposes of evaluating the proposed numerical model (i.e., Figs. 13–15). Direct requests for these materials may be made to the providers, as indicated in the Acknowledgments.

Acknowledgments

This study has been funded by the STAND4HERITAGE project (New Standards for Seismic Assessment of Built Cultural Heritage) that has received funding from the European Research Council (ERC) under the European Union's Horizon 2020 research and innovation program (Grant No. 833123) as an Advanced Grant. Its support is gratefully acknowledged. The opinions and conclusions presented in this paper are those of the authors and do not necessarily reflect the views of the sponsoring organization.

The authors would also like to thank Professor Luigi Sorrentino from the Università degli Studi di Roma "La Sapienza," Rome, Italy, for providing the experimental data reported by Sorrentino et al. (2011) and Al Shawa et al. (2012), as well as Professor Fernando Peña from Universidad Nacional Autónoma de México, Mexico City, Mexico, for providing the experimental data reported by Peña et al. (2008). Their contribution is gratefully acknowledged.

References

Acikgoz, S., and M. J. DeJong. 2012. "The interaction of elasticity and rocking in flexible structures allowed to uplift." *Earthquake Eng. Struct. Dyn.* 41 (15): 2177–2194. https://doi.org/10.1002/eqe.2181.

Al Shawa, O., G. De Felice, A. Mauro, and L. Sorrentino. 2012. "Out-of-plane seismic behaviour of rocking masonry walls." *Earthquake Eng. Struct. Dyn.* 41 (5): 949–968. https://doi.org/10.1002/eqe.1168.

AlShawa, O., D. Liberatore, and L. Sorrentino. 2019. "Dynamic one-sided out-of-plane behavior of unreinforced-masonry wall restrained by elasto-plastic tie-rods." *Int. J. Archit. Heritage* 13 (3): 340–357. https://doi.org/10.1080/15583058.2018.1563226.

AlShawa, O., L. Sorrentino, and D. Liberatore. 2017. "Simulation of shake table tests on out-of-plane masonry buildings. Part II: Combined finite-discrete elements." *Int. J. Archit. Heritage* 11 (1): 79–93. https://doi.org/10.1080/15583058.2016.1237588.

Anagnostopoulos, S. A. 2004. "Equivalent viscous damping for modeling inelastic impacts in earthquake pounding problems." *Earthquake Eng. Struct. Dyn.* 33 (8): 897–902. https://doi.org/10.1002/eqe.377.

Avgenakis, E., and I. N. Psycharis. 2017. "Modeling of rocking elastic flexible bodies under static loading considering the nonlinear stress distribution at their base." *J. Struct. Eng.* 143 (7): 04017051. https://doi.org/10.1061/(ASCE)ST.1943-541X.0001783.

Bachmann, J. A., M. Strand, M. F. Vassiliou, M. Broccardo, and B. Stojadinović. 2018. "Is rocking motion predictable?" *Earthquake Eng. Struct. Dyn.* 47 (2): 535–552. https://doi.org/10.1002/eqe.2978.

Bachmann, J. A., M. F. Vassiliou, and B. Stojadinović. 2017. "Dynamics of rocking podium structures." *Earthquake Eng. Struct. Dyn.* 46 (14): 2499–2517. https://doi.org/10.1002/eqe.2915.

Bao, Y., and D. Konstantinidis. 2020. "Dynamics of a sliding-rocking block considering impact with an adjacent wall." *Earthquake Eng. Struct. Dyn.* 49 (5): 498–523. https://doi.org/10.1002/eqe.3250.

Bruneau, M. 1994. "State-of-the-art report on seismic performance of unreinforced masonry buildings." *J. Struct. Eng.* 120 (1): 230–251. https://doi.org/10.1061/(ASCE)0733-9445(1994)120:1(230).

Cappelli, E., A. Di Egidio, and F. Vestroni. 2020. "Analytical and experimental investigation of the behavior of a rocking masonry tuff wall." *J. Eng. Mech.* 146 (6): 04020048. https://doi.org/10.1061/(ASCE)EM.1943-7889.0001775.

Casapulla, C., L. Giresini, and P. B. Lourenço. 2017. "Rocking and kinematic approaches for rigid block analysis of masonry walls: State of the art and recent developments." *Buildings* 7 (3): 69. https://doi.org/10.3390/buildings7030069.

Charney, F. A. 2008. "Unintended consequences of modeling damping in structures." *J. Struct. Eng.* 134 (4): 581–592. https://doi.org/10.1061/(ASCE)0733-9445(2008)134:4(581).

Chatzis, M. N., M. G. Espinosa, and A. W. Smyth. 2017. "Examining the energy loss in the inverted pendulum model for rocking bodies." *J. Eng. Mech.* 143 (5): 04017013. https://doi.org/10.1061/(ASCE)EM.1943-7889.0001205.

Cheng, C. 2007. "Energy dissipation in rocking bridge piers under free vibration tests." *Earthquake Eng. Struct. Dyn.* 36 (4): 503–518. https://doi.org/10.1002/eqe.640.

Costa, A. A., A. Arêde, A. Penna, and A. Costa. 2013. "Free rocking response of a regular stone masonry wall with equivalent block approach: Experimental and analytical evaluation." *Earthquake Eng. Struct. Dyn.* 42 (15): 2297–2319. https://doi.org/10.1002/eqe.2327.

D'Altri, A. M., V. Sarhosis, G. Milani, J. Rots, S. Cattari, S. Lagomarsino, E. Sacco, A. Tralli, G. Castellazzi, and S. de Miranda. 2019. "Modeling strategies for the computational analysis of unreinforced masonry structures: Review and classification." *Arch. Comput. Methods Eng.* 27 (4): 1153–1185. https://doi.org/10.1007/s11831-019-09351-x.

D'Ayala, D., and E. Speranza. 2003. "Definition of collapse mechanisms and seismic vulnerability of historic masonry buildings." *Earthquake Spectra* 19 (3): 479–509. https://doi.org/10.1193/1.1599896.

de Felice, G., S. De Santis, P. B. Lourenço, and N. Mendes. 2017. "Methods and challenges for the seismic assessment of historic masonry structures." *Int. J. Archit. Heritage* 11 (1): 143–160. https://doi.org/10.1080/15583058.2016.1238976.

DeJong, M. J. 2009. "Seismic assessment strategies for masonry structures." Ph.D. dissertation, Dept. of Architecture, Massachusetts Institute of Technology.

DeJong, M. J., and E. G. Dimitrakopoulos. 2014. "Dynamically equivalent rocking structures." *Earthquake Eng. Struct. Dyn.* 43 (10): 1543–1563. https://doi.org/10.1002/eqe.2410.

Derakhshan, H., M. C. Griffith, and J. M. Ingham. 2013. "Out-of-plane behavior of one-way spanning unreinforced masonry walls." *J. Eng. Mech.* 139 (4): 409–417. https://doi.org/10.1061/(ASCE)EM.1943-7889.0000347.

DIANA. 2017. *User's manual—Release 10.1*. Delft, Netherlands: DIANA FEA BV.

Di Egidio, A., and A. Contento. 2009. "Base isolation of slide-rocking non-symmetric rigid blocks under impulsive and seismic excitations." *Eng. Struct.* 31 (11): 2723–2734. https://doi.org/10.1016/j.engstruct.2009.06.021.

Doherty, K., M. C. Griffith, N. Lam, and J. Wilson. 2002. "Displacement-based seismic analysis for out-of-plane bending of unreinforced masonry walls." *Earthquake Eng. Struct. Dyn.* 31 (4): 833–850. https://doi.org/10.1002/eqe.126.

ElGawady, M., Q. Ma, J. Butterworth, and J. Ingham. 2011. "Effects of interface material on the performance of free rocking blocks." *Earthquake Eng. Struct. Dyn.* 40 (4): 375–392. https://doi.org/10.1002/eqe.1025.

Giannini, R., and R. Masiani. 1990. "Risposta in frequenza del blocco rigido: Stabilita delle soluzioni." In *Proc., 10th Italian National Conf. of Theoretical and Applied Mechanics*. Pisa, Italy: European Turfgrass Society.

Giordano, N., F. De Luca, and A. Sextos. 2020. "Out-of-plane closed-form solution for the seismic assessment of unreinforced masonry schools in Nepal." *Eng. Struct.* 203 (Jan): 109548. https://doi.org/10.1016/j.engstruct.2019.109548.

Giouvanidis, A. I., and E. G. Dimitrakopoulos. 2017a. "Nonsmooth dynamic analysis of sticking impacts in rocking structures." *Bull. Earthquake Eng.* 15 (5): 2273–2304. https://doi.org/10.1007/s10518-016-0068-4.

Giouvanidis, A. I., and E. G. Dimitrakopoulos. 2017b. "Seismic performance of rocking frames with flag-shaped hysteretic behavior." *J. Eng. Mech.* 143 (5): 04017008. https://doi.org/10.1061/(ASCE)EM.1943-7889.0001206.

Giouvanidis, A. I., and E. G. Dimitrakopoulos. 2018. "Rocking amplification and strong-motion duration." *Earthquake Eng. Struct. Dyn.* 47 (10): 2094–2116. https://doi.org/10.1002/eqe.3058.

Giouvanidis, A. I., and Y. Dong. 2020. "Seismic loss and resilience assessment of single-column rocking bridges." *Bull. Earthquake Eng.* 18 (9): 4481–4513. https://doi.org/10.1007/s10518-020-00865-5.

Giresini, L., M. Fragiacomo, and P. B. Lourenço. 2015. "Comparison between rocking analysis and kinematic analysis for the dynamic out-of-plane behavior of masonry walls." *Earthquake Eng. Struct. Dyn.* 44 (13): 2359–2376. https://doi.org/10.1002/eqe.2592.

Giresini, L., and M. Sassu. 2017. "Horizontally restrained rocking blocks: Evaluation and dynamic approaches." *Bull. Earthquake Eng.* 15 (1): 385–410. https://doi.org/10.1007/s10518-016-9967-7.

Godio, M., and K. Beyer. 2017. "Analytical model for the out-of-plane response of vertically spanning unreinforced masonry walls." *Earthquake Eng. Struct. Dyn.* 46 (15): 2757–2776. https://doi.org/10.1002/eqe.2929.

Godio, M., and K. Beyer. 2019. "Evaluation of force-based and displacement-based out-of-plane seismic assessment methods for unreinforced masonry walls through refined model simulations." *Earthquake Eng. Struct. Dyn.* 48 (4): 454–475. https://doi.org/10.1002/eqe.3144.

Griffith, M. C., N. Lam, J. L. Wilson, and K. Doherty. 2004. "Experimental investigation of unreinforced brick masonry walls in flexure." *J. Struct. Eng.* 130 (3): 423–432. https://doi.org/10.1061/(ASCE)0733-9445(2004)130:3(423).

Hall, J. F. 2006. "Problems encountered from the use (or misuse) of Rayleigh damping." *Earthquake Eng. Struct. Dyn.* 35 (5): 525–545. https://doi.org/10.1002/eqe.541.

Hilber, H. M., T. J. R. Hughes, and R. L. Taylor. 1977. "Algorithms in structural dynamics." *Earthquake Eng. Struct. Dyn.* 5 (3): 283–292. https://doi.org/10.1002/eqe.4290050306.

Hogan, S. J. 1992. "The effect of damping on rigid block motion under harmonic forcing." *Proc. R. Soc. London, Ser. A* 437 (1899): 97–108. https://doi.org/10.1098/rspa.1992.0049.

Housner, G. W. 1963. "The behavior of inverted pendulum structures during earthquakes." *Bull. Seismol. Soc. Am.* 53 (2): 403–417.

Imanishi, N., Y. Inoue, and K. Shibata. 2012. "Effect of base shape on damping of rocking of rigid body." *J. Syst. Des. Dyn.* 6 (1): 109–119. https://doi.org/10.1299/jsdd.6.109.

Ingham, J., and M. Griffith. 2011. "Performance of unreinforced masonry buildings during the 2010 Darfield (Christchurch, NZ) earthquake." *Aust. J. Struct. Eng.* 11 (3): 207–224. https://doi.org/10.1080/13287982.2010.11465067.

Itasca. 2013. *3DEC—3 dimensional distinct element code*. Minneapolis: Itasca Consulting Group.

Kalliontzis, D., and S. Sritharan. 2018. "Characterizing dynamic decay of motion of free-standing rocking members." *Earthquake Spectra* 34 (2): 843–866. https://doi.org/10.1193/011217EQS013M.

Kalliontzis, D., S. Sritharan, and A. Schultz. 2016. "Improved coefficient of restitution estimation for free rocking members." *J. Struct. Eng.* 142 (12): 06016002. https://doi.org/10.1061/(ASCE)ST.1943-541X.0001598.

Lemos, J. V. 2019. "Discrete element modeling of the seismic behavior." *Buildings* 9 (2): 43. https://doi.org/10.3390/buildings9020043.

Lemos, J. V., and A. Campos Costa. 2017. "Simulation of shake table tests on out-of-plane masonry buildings. Part V: Discrete element approach." *Int. J. Archit. Heritage* 11 (1): 117–124. https://doi.org/10.1080/15583058.2016.1238973.

Lipscombe, P. R., and S. Pellegrino. 1993. "Free rocking of prismatic blocks." *J. Eng. Mech.* 119 (7): 1387–1410. https://doi.org/10.1061/(ASCE)0733-9399(1993)119:7(1387).

Lourenço, P. B., D. V. Oliveira, P. Roca, and A. Orduña. 2005. "Dry joint stone masonry walls subjected to in-plane combined loading." *J. Struct. Eng.* 131 (11): 1665–1673. https://doi.org/10.1061/(ASCE)0733-9445(2005)131:11(1665).

Makris, N. 2014. "The role of the rotational inertia on the seismic resistance of free-standing rocking columns and articulated frames." *Bull. Seismol. Soc. Am.* 104 (5): 2226–2239. https://doi.org/10.1785/0120130064.

Makris, N., and D. Konstantinidis. 2003. "The rocking spectrum and the limitations of practical design methodologies." *Earthquake Eng. Struct. Dyn.* 32 (2): 265–289. https://doi.org/10.1002/eqe.223.

Malomo, D., A. Mehrotra, and M. J. DeJong. 2021. "Distinct element modeling of the dynamic response of a rocking podium tested on a shake table." *Earthquake Eng. Struct. Dyn.* 50 (5): 1469–1475. https://doi.org/10.1002/eqe.3404.

MathWorks. 1992. *MATLAB: The language of technical computing*. Natick, MA: MathWorks.

Mauro, A., G. de Felice, and M. J. DeJong. 2015. "The relative dynamic resilience of masonry collapse mechanisms." *Eng. Struct.* 85 (Feb): 182–194. https://doi.org/10.1016/j.engstruct.2014.11.021.

Mehrotra, A., and M. J. DeJong. 2018. "The influence of interface geometry, stiffness, and crushing on the dynamic response of masonry collapse mechanisms." *Earthquake Eng. Struct. Dyn.* 47 (13): 2661–2681. https://doi.org/10.1002/eqe.3103.

Mehrotra, A., and M. J. DeJong. 2020. "A methodology to account for interface flexibility and crushing effects in multi-block masonry collapse mechanisms." *Meccanica* 55 (6): 1237–1261. https://doi.org/10.1007/s11012-020-01161-x.

Peña, F., P. B. Lourenço, and A. Campos-Costa. 2008. "Experimental dynamic behavior of free-standing multi-block structures under seismic loadings." *J. Earthquake Eng.* 12 (6): 953–979. https://doi.org/10.1080/13632460801890513.

Penna, A., P. Morandi, M. Rota, C. F. Manzini, F. da Porto, and G. Magenes. 2014. "Performance of masonry buildings during the Emilia 2012 earthquake." *Bull. Earthquake Eng.* 12 (5): 2255–2273. https://doi.org/10.1007/s10518-013-9496-6.

Portioli, F., and L. Cascini. 2018. "Contact dynamics of masonry block structures using mathematical programming." *J. Earthquake Eng.* 22 (1): 94–125. https://doi.org/10.1080/13632469.2016.1217801.

Priestley, M. J. N., R. J. Evison, and A. J. Carr. 1978. "Seismic response of structures free to rock on their foundations." *Bull. N.Z. Soc. Earthquake Eng.* 11 (3): 141–150. https://doi.org/10.5459/bnzsee.11.3.141-150.

Psycharis, I. N., M. Fragiadakis, and I. Stefanou. 2013. "Seismic reliability assessment of classical columns subjected to near-fault ground motions." *Earthquake Eng. Struct. Dyn.* 42 (14): 2061–2079. https://doi.org/10.1002/eqe.2312.

Pulatsu, B., E. Erdogmus, and P. B. Lourenço. 2019. "Comparison of in-plane and out-of-plane failure modes of masonry arch bridges using discontinuum analysis." *Eng. Struct.* 178 (Oct): 24–36. https://doi.org/10.1016/j.engstruct.2018.10.016.

Routledge, P., B. Mchaffie, M. Cowan, and A. Palermo. 2020. "Wigram—Magdala link bridge: Low-damage details for a more efficient seismic design philosophy." *Struct. Eng. Int.* 30 (2): 177–184. https://doi.org/10.1080/10168664.2019.1679696.

Sarhosis, V., D. Baraldi, J. V. Lemos, and G. Milani. 2019. "Dynamic behaviour of ancient freestanding multi-drum and monolithic columns subjected to horizontal and vertical excitations." *Soil Dyn. Earthquake Eng.* 120 (May): 39–57. https://doi.org/10.1016/j.soildyn.2019.01.024.

Simulia. 2012. *ABAQUS 6.12 documentation*. Johnston, RI: Dassault Systèmes Simulia.

Sorrentino, L., O. AlShawa, and L. D. Decanini. 2011. "The relevance of energy damping in unreinforced masonry rocking mechanisms: Experimental and analytic investigations." *Bull. Earthquake Eng.* 9 (5): 1617–1642. https://doi.org/10.1007/s10518-011-9291-1.

Sorrentino, L., D. D'Ayala, G. de Felice, M. C. Griffith, S. Lagomarsino, and G. Magenes. 2017. "Review of out-of-plane seismic assessment techniques applied to existing masonry buildings." *Int. J. Archit. Heritage* 11 (1): 2–21. https://doi.org/10.1080/15583058.2016.1237586.

Spanos, P. D., A. Di Matteo, A. Pirrotta, and M. Di Paola. 2017. "Rocking of rigid block on nonlinear flexible foundation." *Int. J. Non Linear Mech.* 94 (Sep): 362–374. https://doi.org/10.1016/j.ijnonlinmec.2017.06.005.

Spanos, P. D., P. C. Roussis, and N. P. A. Politis. 2001. "Dynamic analysis of stacked rigid blocks." *Soil Dyn. Earthquake Eng.* 21 (7): 559–578. https://doi.org/10.1016/S0267-7261(01)00038-0.

Ther, T., and L. P. Kollar. 2017. "Refinement of Housner's model on rocking blocks." *Bull. Earthquake Eng.* 15 (5): 2305–2319. https://doi.org/10.1007/s10518-016-0048-8.

Tomassetti, U., F. Graziotti, L. Sorrentino, and A. Penna. 2019. "Modelling rocking response via equivalent viscous damping." *Earthquake Eng. Struct. Dyn.* 48 (11): 1277–1296. https://doi.org/10.1002/eqe.3182.

Vaculik, J., M. C. Griffith, and G. Magenes. 2014. "Dry stone masonry walls in bending. Part II: Analysis." *Int. J. Archit. Heritage* 8 (1): 29–48. https://doi.org/10.1080/15583058.2012.663060.

Vassiliou, M. F., S. Gunay, B. Stojadinovic, M. Broccardo, K. M. Mosalam, C. Cengiz, M. Dietz, L. Dihoru, G. Mylonakis, and A. Sextos. 2021. "Shake table testing of a rocking podium: Results of a blind prediction contest." *Earthquake Eng. Struct. Dyn.* 50 (4): 1043–1062. https://doi.org/10.1002/eqe.3386.

Vassiliou, M. F., K. R. Mackie, and B. Stojadinović. 2014. "Dynamic response analysis of solitary flexible rocking bodies: Modeling and behavior under pulse-like ground excitation." *Earthquake Eng. Struct. Dyn.* 43 (10): 1463–1481. https://doi.org/10.1002/eqe.2406.

Vlachakis, G., E. Vlachaki, and P. B. Lourenço. 2020. "Learning from failure: Damage and failure of masonry structures, after the 2017 Lesvos earthquake (Greece)." *Eng. Fail. Anal.* 117 (Nov): 104803. https://doi.org/10.1016/j.engfailanal.2020.104803.